PREPARATION AND OPERATIONS OF THE MISSION PERFORMANCE CENTRE (MPC) FOR THE COPERNICUS SENTINEL-3 MISSION

S3-A OLCI Cyclic Performance Report

Cycle No. 023

Start date: 30/09/2017

End date: 27/10/2017

SENTINEL 3

Mission Performance Centre

Ref.: S3MPC.ACR.PR.01-023
Issue: 1.0
Date: 06/11/2017
Contract: 4000111836/14/I-LG

Customer:	ESA	**Document Ref.:**	S3MPC.ACR.PR.01-023
Contract No.:	4000111836/14/I-LG	**Date:**	06/11/2017
		Issue:	1.0

Project:	PREPARATION AND OPERATIONS OF THE MISSION PERFORMANCE CENTRE (MPC) FOR THE COPERNICUS SENTINEL-3 MISSION		
Title:	S3-A OLCI Cyclic Performance Report		
Author(s):	OLCI ESLs		
Approved by:	L. Bourg, OLCI ESL Coordinator	**Authorized by**	Frédéric Rouffi, OPT Technical Performance Manager
Distribution:	ESA, EUMETSAT, S3MPC consortium		
Accepted by ESA	S. Dransfeld, MPC Deputy TO for OPT P. Féménias, MPC TO		
Filename	S3MPC.ACR.PR.01-023 - i1r0 - OLCI Cyclic Report 023.docx		

Disclaimer

The work performed in the frame of this contract is carried out with funding by the European Union. The views expressed herein can in no way be taken to reflect the official opinion of either the European Union or the European Space Agency.

Changes Log

Version	Date	Changes
1.0	06/11/2017	First Version

List of Changes

Version	Section	Answers to RID	Changes

Table of content

TABLE OF CONTENT ..... **IV**

LIST OF FIGURES ..... **V**

1 INSTRUMENT MONITORING **1**

1.1 CCD TEMPERATURES 1
1.2 RADIOMETRIC CALIBRATION 2
1.2.1 Dark Offsets [OLCI-L1B-CV-230] *4*
1.2.2 Instrument response and degradation modelling [OLCI-L1B-CV-250] *9*
1.2.3 Ageing of nominal diffuser [OLCI-L1B-CV-240] *17*
1.2.4 Updating of calibration ADF [OLCI-L1B-CV-260] *19*
1.2.5 Radiometric Calibrations for sun azimuth angle dependency and Yaw Manoeuvres for Solar Diffuser on-orbit re-characterization [OLCI-L1B-CV-270 and OLCI-L1B-CV-280] *19*
1.3 SPECTRAL CALIBRATION [OLCI-L1B-CV-400] 19
1.4 SIGNAL TO NOISE ASSESSMENT [OLCI-L1B-CV-620] 19
1.4.1 SNR from Radiometric calibration data *19*
1.4.2 SNR from EO data *22*
1.5 GEOMETRIC CALIBRATION/VALIDATION 22

2 OLCI LEVEL 1 PRODUCT VALIDATION **26**

2.1 [OLCI-L1B-CV-300], [OLCI-L1B-CV-310] – RADIOMETRIC VALIDATION 26
2.1.1 S3ETRAC Service *26*
2.1.2 Radiometric validation with DIMITRI *27*
2.1.3 Radiometric validation with OSCAR *32*
2.2 [OLCI-L1B-CV-320] – RADIOMETRIC VALIDATION WITH LEVEL 3 PRODUCTS 33

3 LEVEL 2 LAND PRODUCTS VALIDATION **34**

3.1 [OLCI-L2LRF-CV-300] 34
3.2 [OLCI-L2LRF-CV-410 & OLCI-L2LRF-CV-420] – CLOUD MASKING & SURFACE CLASSIFICATION FOR LAND PRODUCTS 39
3.3 VALIDATION OF INTEGRATED WATER VAPOUR OVER LAND 39

4 LEVEL 2 WATER PRODUCTS VALIDATION **40**

4.1 [OLCI-L2-CV-210, OLCI-L2-CV-220] – VICARIOUS CALIBRATION OF THE NIR AND VIS BANDS 40
4.2 [OLCI-L2WLR-CV-300, OLCI-L2WLR-CV-310, OLCI-L2WLR-CV-32, OLCI-L2WLR-CV-330, OLCI-L2WLR-CV-340, OLCI-L2WLR-CV-350, OLCI-L2WLR-CV-360 AND OLCI-L2WLR-CV-370] – LEVEL 2 WATER-LEAVING REFLECTANCE PRODUCT VALIDATION 40
4.3 [OLCI-L2WLR-CV530] VALIDATION OF AEROSOL PRODUCT 44
4.4 [OLCI-L2WLR-CV-380] DEVELOPMENT OF CALIBRATION, PRODUCT AND SCIENCE ALGORITHMS 45

5 LEVEL 2 SYN PRODUCTS VALIDATION **46**

5.1 [SYN-L2-CV-100] 46

6 EVENTS **47**

7 APPENDIX A **48**

List of Figures

Figure 1: long term monitoring of CCD temperatures using minimum value (top), time averaged values (middle), and maximum value (bottom) provided in the annotations of the Radiometric Calibration Level 1 products, for the Shutter frames, all radiometric calibrations so far. ---------- 1

Figure 2: Same as Figure 1 for diffuser frames. ---------- 2

Figure 3: Sun azimuth angles during acquired Radiometric Calibrations (diffuser frame) on top of nominal yearly cycle (black curve). Diffuser 1 with diamonds, diffuser 2 with crosses, 2016 acquisitions in blue, 2017 in red. ---------- 3

Figure 4: Sun geometry during radiometric Calibrations on top of characterization ones (diffuser frame) 3

Figure 5: Dark Offset table for band Oa06 with (red) and without (black) HEP filtering (Radiometric Calibration of 22 July 2017). The strong HEP event near pixel 400 has been detected and removed by the HEP filtering. ---------- 4

Figure 6: Dark Offset for band Oa1 (top) and Oa21 (bottom), all radiometric calibrations so far except the first one (orbit 183) for which the instrument was not thermally stable yet. ---------- 5

Figure 7: map of periodic noise for the 5 cameras, for band Oa21. X-axis is detector number (East part, from 540 to 740, where the periodic noise occurs), Y-axis is the orbit number. The counts have been corrected from the west detectors mean value (not affected by periodic noise) in order to remove mean level gaps and consequently to have a better visualisation of the long term evolution of the periodic noise structure. Periodic noise amplitude is high in camera 2, 3 and 4. It is lower in camera 4 and small in camera 1. ---------- 6

Figure 8: same as Figure 7 for smear band. ---------- 6

Figure 9: Dark Offset levels for smear band camera 5, for (left plot) first 30 WEST detectors including virtual and blind pixels, (right plot) last 30 EAST detectors including blind pixels. The color of the curves is linked to the orbit number, from the beginning of the mission in black, to the last CALs in red. We see on the right plot that the shape of the PN for the very last CAL (orbit 8736) has been strongly modified by the reset of the OLCI instrument of orbit 8666.As a consequence, the global mean level of the dark offset is impacted by this change of PN, through the OCL convergence, as illustrated in the left plot.----- 7

Figure 10: Dark Current for band Oa1 (top) and Oa21 (bottom), all radiometric calibrations so far except the first one (orbit 183) for which the instrument was not thermally stable yet. ---------- 8

Figure 11: left column: ACT mean on 400 first detectors of Dark Current coefficients for spectral band Oa01 (top) and Oa21 (bottom). Right column: same as left column but for Standard deviation instead of mean. We see an increase of the DC level as a function of time especially for band Oa21. A possible explanation could be the increase of the number of hot pixels which is more important in Oa21 because this band is made of more CCD lines than band Oa01 and thus receives more cosmic rays impacts. It is known that cosmic rays degrade the structure of the CCD, generating more and more hot pixels at long term scales. ---------- 8

Figure 12: Gain Coefficients for band Oa1 (top) and Oa21 (bottom), all diffuser 1 radiometric calibrations so far except the first one (orbit 183) for which the instrument was not thermally stable yet. ---------- 9

Figure 13: camera averaged gain relative evolution with respect to “best geometry” calibration (22/11/2016), as a function of elapsed time since launch; one curve for each band (see colour code on plots), one plot for each module. The star tracker anomaly fix (6/04/16) is represented by a vertical red dashed line. ----------10

Figure 14: RMS performance of the Gain Model of current Processing Baseline as a function of orbit.---11

Figure 15: RMS performance of the Gain Model of previous Processing Baseline as a function of orbit. -11

Figure 16: Camera-averaged instrument evolution since channel programming change (25/04/2016) and up to most recent calibration (21/10/2017) versus wavelength. ----------12

Figure 17: For the 5 cameras: Evolution model performance, as camera-average and standard deviation of ratio of Model over Data vs. wavelength, for each orbit of the test dataset, including 4 calibration in extrapolation, with a colour code for each calibration from blue (oldest) to red (most recent).----------13

Figure 18: Evolution model performance, as ratio of Model over Data vs. pixels, all cameras side by side, over the whole current calibration dataset (since instrument programing update), including 4 calibrations in extrapolation, channels Oa1 to Oa6. ----------14

Figure 19: same as Figure 14 for channels Oa7 to Oa14. ----------15

Figure 20: same as Figure 18 for channels Oa15 to Oa21.----------16

Figure 21 : FOV-averaged ageing for each band (see colour code) vs time (top) and cumulated exposures (bottom).----------17

Figure 22 : cumulated exposure versus time (absolute orbit). The steep slope around orbit 4200 corresponds to the Yaw Manoeuvres.----------18

Figure 23 : intercept and slopes of ageing fits (black and green lines respectively, referring to left axis), and correlation coefficients (red, referring to right axis) versus wavelength. ----------18

Figure 24: Signal to Noise ratio as a function of the spectral band for the 5 cameras. These results have been computed from radiometric calibration data. All calibrations except first one (orbit 183) are presents with the colours corresponding to the orbit number (see legend). The SNR is very stable with time: the curves for all orbits are almost superimposed. The dashed curve is the ESA requirement. -----20

Figure 25: long-term stability of the SNR estimates from Calibration data, example of channel Oa1.-----21

Figure 26: histograms of geolocation errors for the along-track (left) and across-track (right) directions, examples of 01/10/2017 (top) and 26/10/2017 (bottom).----------23

Figure 27: georeferencing error in along-track (left) and across-track (right) directions for all the GCPs, examples of 01/10/2017 (top) and 26/10/2017 (bottom). Note that the symbol size in bottom figure is linked to the lower number of GCPs. ----------24

Figure 28: time series of geolocation errors for the along-track (blue) and across-track (red) directions over 15.6 months. ----------25

Figure 29: summary of S3ETRAC products generation for OLCI (number of OLCI L1 products Ingested, yellow – number of S3ETRAC extracted products generated, blue – number of S3ETRAC runs without

generation of output product (data not meeting selection requirements), green – number of runs ending in error, red, one plot per site type). ----------27

Figure 30: Time-series of the elementary ratios (observed/simulated) signal from S3A/OLCI for (top to bottom) bands Oa03, Oa8 and Oa17 respectively over Six PICS Cal/Val sites. Dashed-green and orange lines indicate the 2% and 5% respectively. Error bars indicate the desert methodology uncertainty. -----28

Figure 31: The estimated gain values for S3A/OLCI over the 6 PICS sites identified by CEOS over the period April 2016 – October 2017 as a function of wavelength. Dashed-green and orange lines indicate the 2% and 5% respectively. Error bars indicate the desert methodology uncertainty. ----------29

Figure 32: Time-series of the elementary ratios (observed/simulated) signal from (black) S2A/MSI, (blue) S3A/OLCI for band Oa17 (865nm) over the LIBYA4 site. Dashed-green and orange lines indicate the 2% and 5% respectively. Error bars indicate the desert methodology uncertainty. ----------30

Figure 33: The estimated gain values (observed-signal /simulated-signal) averaged over different period from different sensors over PICS as function of wavelength. The number of used-acquisitions for each sensor within the period July 2015-October 2017 is indicated in the plot-legend. ----------30

Figure 34: The estimated gain values for S3A/OLCI over the 6 Ocean CalVal sites (Atl-NW_Optimum, Atl-SW_Optimum, Pac-NE_Optimum, Pac-NW_Optimum, SPG_Optimum and SIO_Optimum) over the period December 2016 – October 2017 as a function of wavelength. Dashed-green, and orange lines indicate the 2%, 5% respectively. Error bars indicate the methodology uncertainty. ----------31

Figure 35: The estimated gain values for S3A/OLCI from Glint, Rayleigh and PICS over the period April 2016 – October 2017 for PICS and December 2016-October 2017 for Rayleigh and Glint methods as a function of wavelength. We use the gain value of Oa8 from PICS method as reference gain for Glint. Dashed-green and orange lines indicate the 2% and 5% respectively. Error bars indicate the methods uncertainties. ----------31

Figure 36: OSCAR Rayleigh results for August and September (preliminary) 2017. ----------32

Figure 37: RGB composites of the study sites. A) France B) Los Angles C) Queensland, Australia D) Denmark E) Greenland F) Congo G) Rondonia ----------34

Figure 38: A) RGB image of the River Rhone, France (43°32’02” N, 4°43’06’’ E). B) Inland water flagged pixels. C) Cloud flagged Pixels. D) Pixels classified as both inland water and cloud.----------36

Figure 39: RGB and OTCI bands for Queensland Australia (17°26’04” S, 143°47’15” E).----------37

Figure 40: A) Histogram of OTCI values for cloud pixels. B) Histogram of OTCI values for bare soil pixels.37

Figure 41: Spectral signals of the different classifications within the image Queensland Australia (17°26’04” S, 143°47’15” E).----------38

Figure 42: A) RGB image of Death Valley (38°13’40” N, 116°16’25” W). B) Cloud mask. ----------38

Figure 43: A) RGB composite (39°39’01” N, 115°54’46” W) B) Cloud mask C) Location of Pins. D) Spectral signals of the different pins. ----------39

Figure 44: Scatter plots of OLCI versus in situ radiometry (FR data) ----------41

Figure 45: OLCI and AERONET-OC radiometric time on USCSeaprism station. ----------44

1 Instrument monitoring

1.1 CCD temperatures

The monitoring of the CCD temperatures is based on MPMF data extractions not yet operational. In the meantime, we monitor the CCD temperatures on the long-term using Radiometric Calibration Annotations (see Figure 1). Variations are very small (0.09 C peak-to-peak) and no trend can be identified. Data from current cycle (rightmost data points) do not show any specificity.

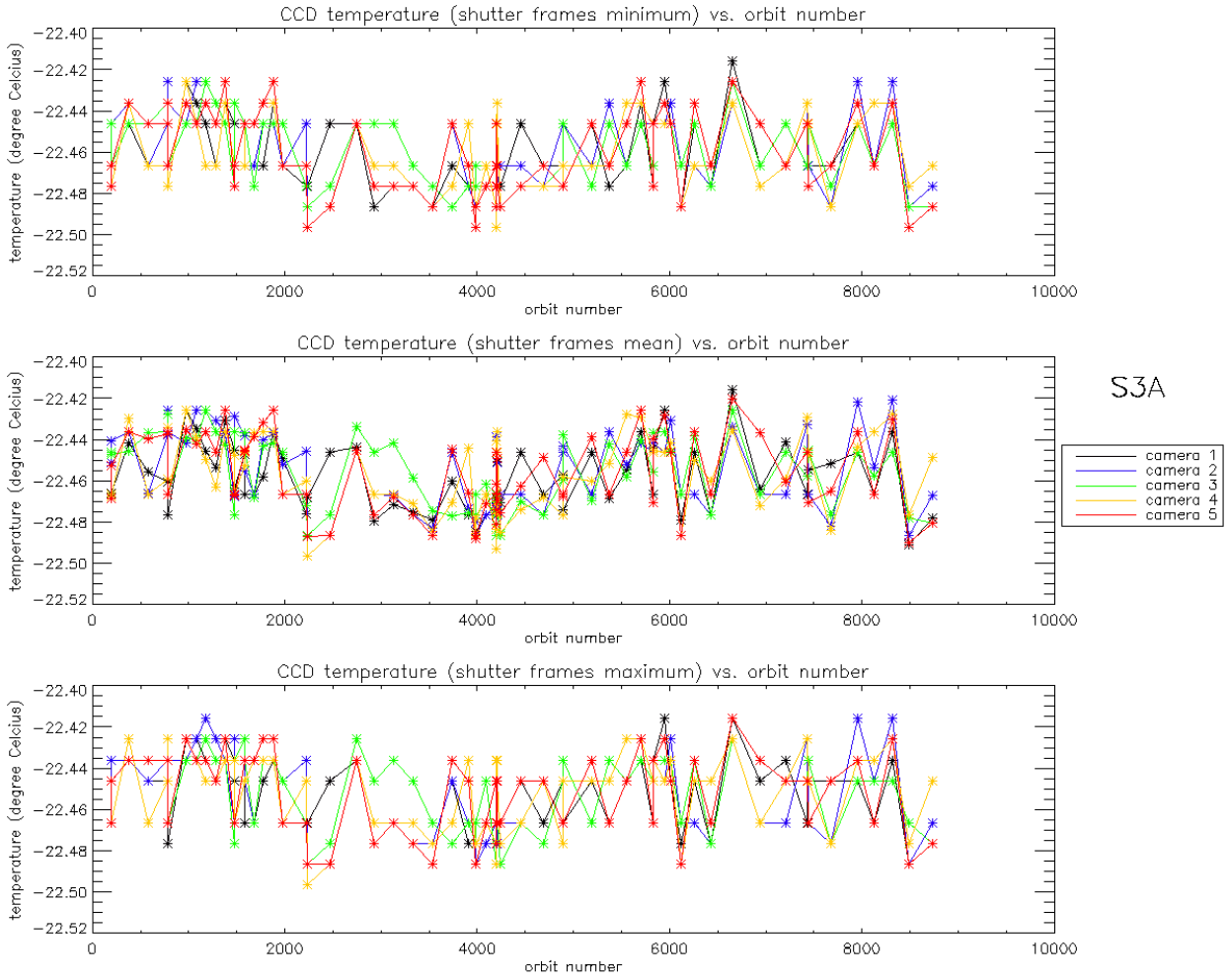

Figure 1: long term monitoring of CCD temperatures using minimum value (top), time averaged values (middle), and maximum value (bottom) provided in the annotations of the Radiometric Calibration Level 1 products, for the Shutter frames, all radiometric calibrations so far.

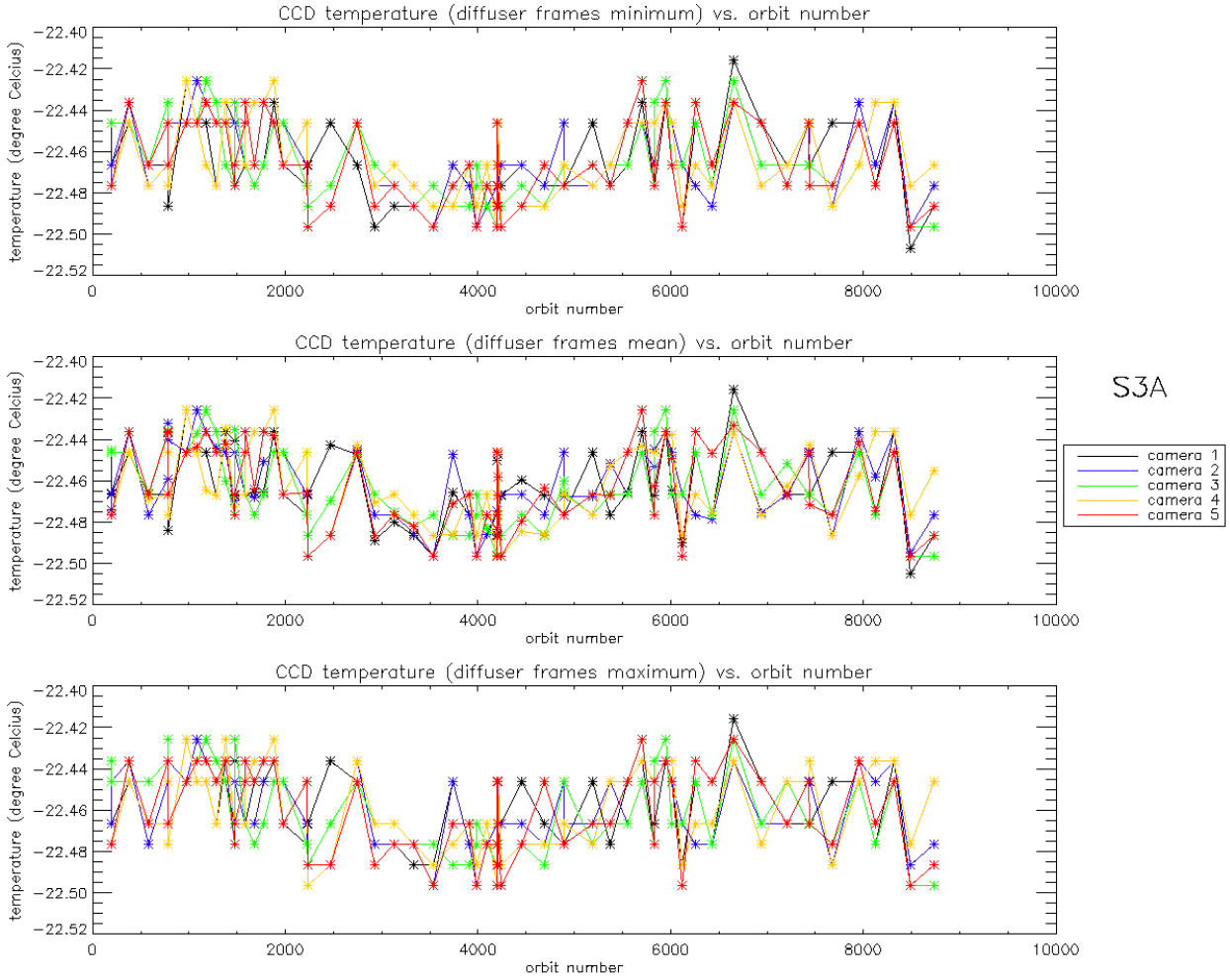

Figure 2: Same as Figure 1 for diffuser frames.

1.2 Radiometric Calibration

Two OLCI Radiometric Calibration Sequences have been acquired during Cycle 023:

- S01 sequence (diffuser 1) on 04/10/2017 07:58 to 08:00 (absolute orbit 8492)
- S01 sequence (diffuser 1) on 21/10/2017 10:41 to 10:43 (absolute orbit 8736)

The acquired Sun azimuth angles are presented on below, on top of the nominal values without Yaw Manoeuvre (i.e. with nominal Yaw Steering control of the satellite).

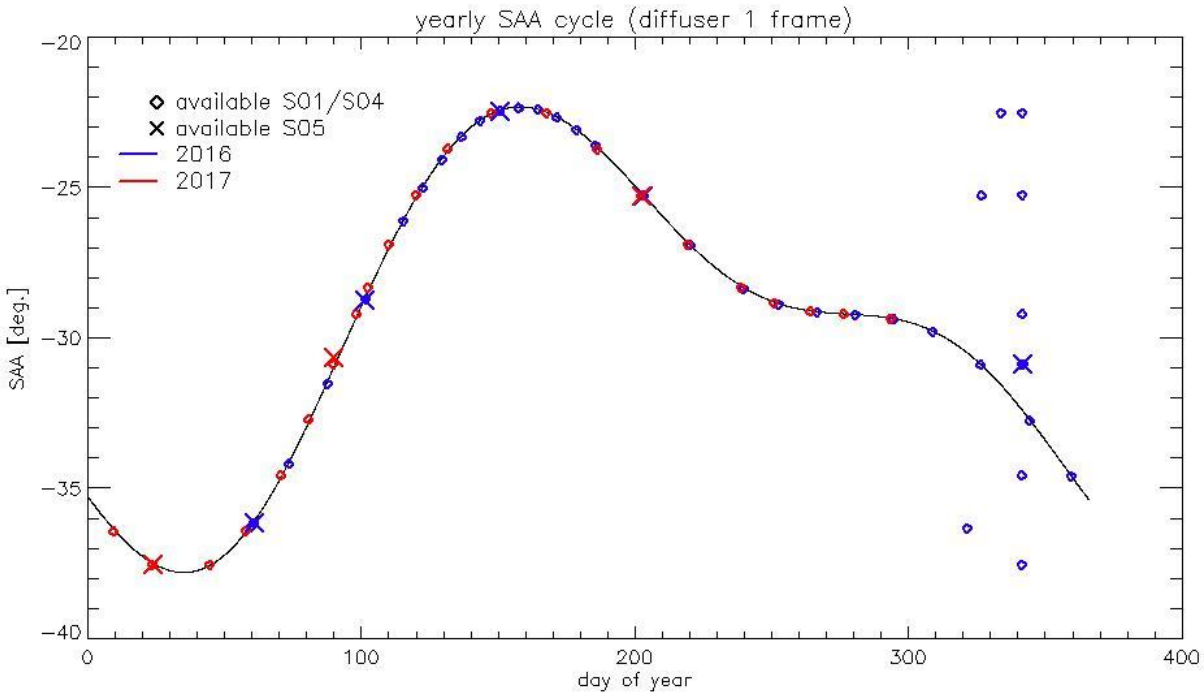

Figure 3: Sun azimuth angles during acquired Radiometric Calibrations (diffuser frame) on top of nominal yearly cycle (black curve). Diffuser 1 with diamonds, diffuser 2 with crosses, 2016 acquisitions in blue, 2017 in red.

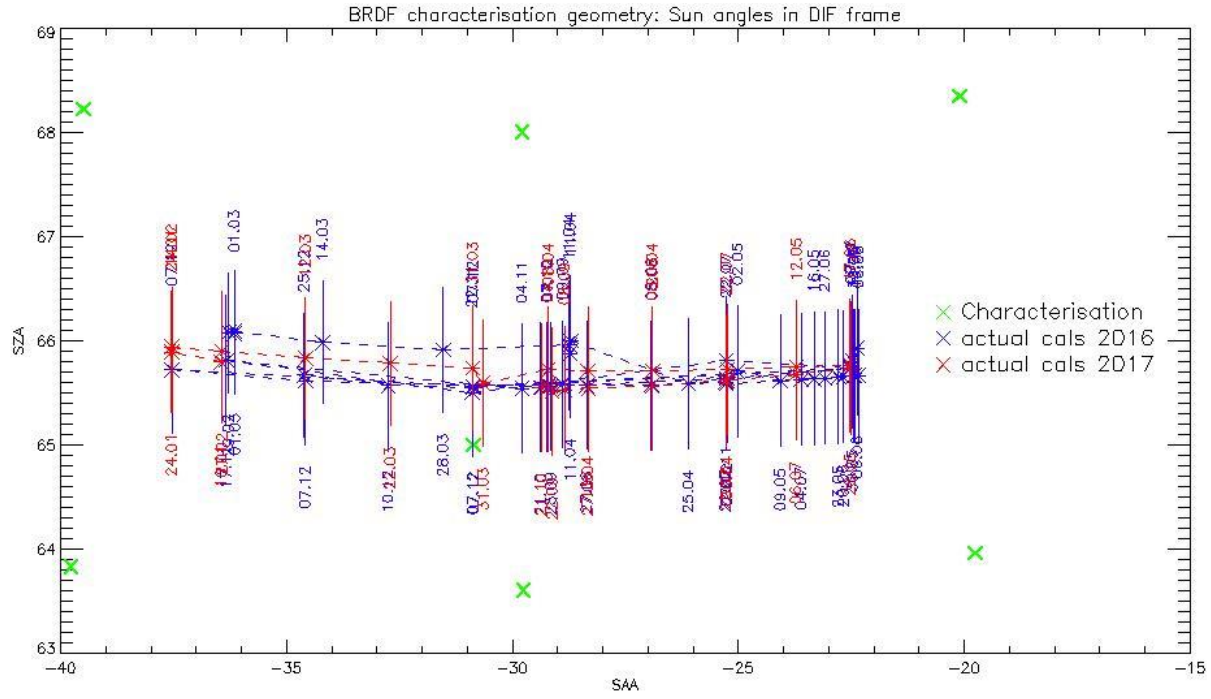

Figure 4: Sun geometry during radiometric Calibrations on top of characterization ones (diffuser frame)

This section presents the overall monitoring of the parameters derived from radiometric calibration data and highlights, if present, specificity of current cycle data.

1.2.1 Dark Offsets [OLCI-L1B-CV-230]

Note about the High Energy Particles:

The filtering of High Energy Particle (HEP) events from radiometric calibration data has been implemented (for shutter frames only) in a post processor, allowing generating Dark Offset and Dark Current tables computed on filtered data. The post-processor starts from IPF intermediate data (corrected counts), applies the HEP detection and filtering and finally computes the Dark Offset and Dark Current tables the same way as IPF. An example of the impact of HEP filtering is given in Figure 5.

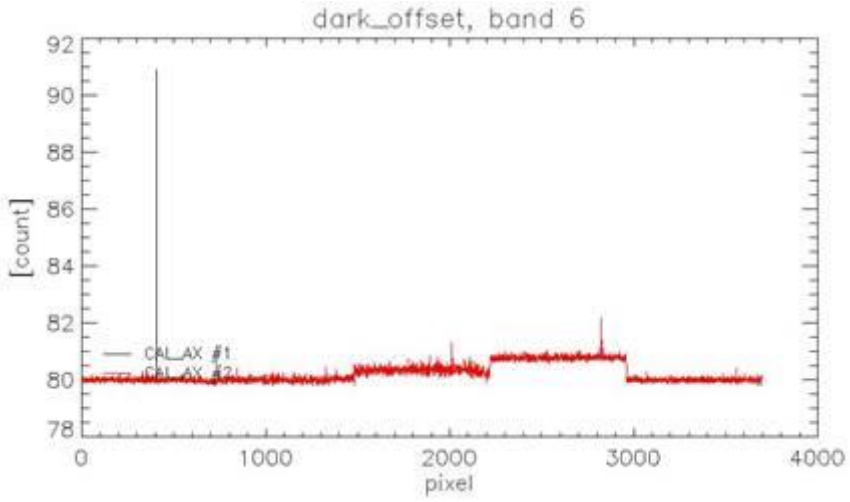

Figure 5: Dark Offset table for band Oa06 with (red) and without (black) HEP filtering (Radiometric Calibration of 22 July 2017). The strong HEP event near pixel 400 has been detected and removed by the HEP filtering.

All results presented below in this section have been obtained using the HEP filtered Dark Offset and Dark Current tables.

Dark offsets

Dark offsets are continuously affected by the global offset induced by the Periodic Noise on the OCL convergence. Current Cycle calibrations are affected the same way as others. The amplitude of the shift varies with band and camera from virtually nothing (e.g. camera 2, band 0a1) to up to 5 counts (Oa21, camera 3). The Periodic Noise itself comes on top of the global shift with its known signature: high frequency oscillations with a rapid damp. This effect remains more or less stable with time in terms of amplitude, frequency and decay length, but its phase varies with time, introducing the global offset mentioned above.

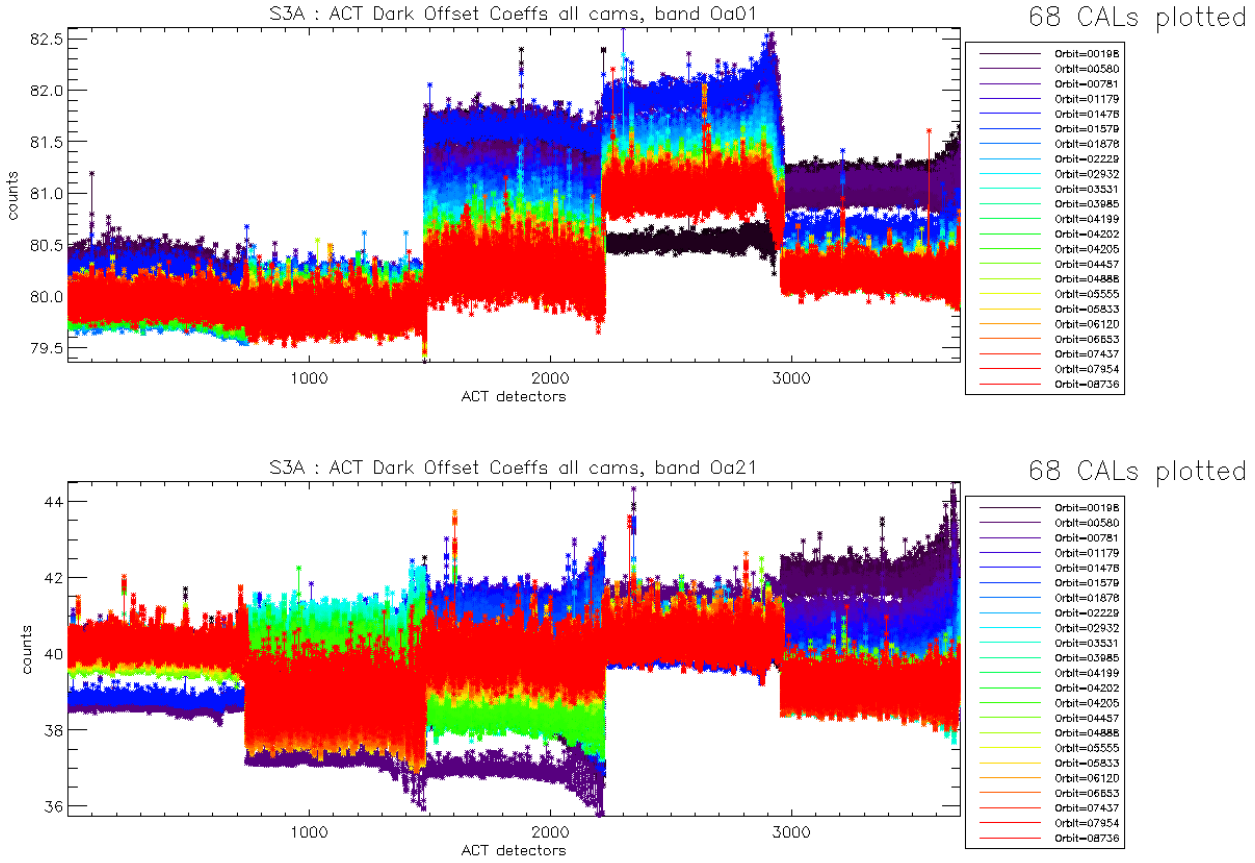

Figure 6: Dark Offset for band Oa1 (top) and Oa21 (bottom), all radiometric calibrations so far except the first one (orbit 183) for which the instrument was not thermally stable yet.

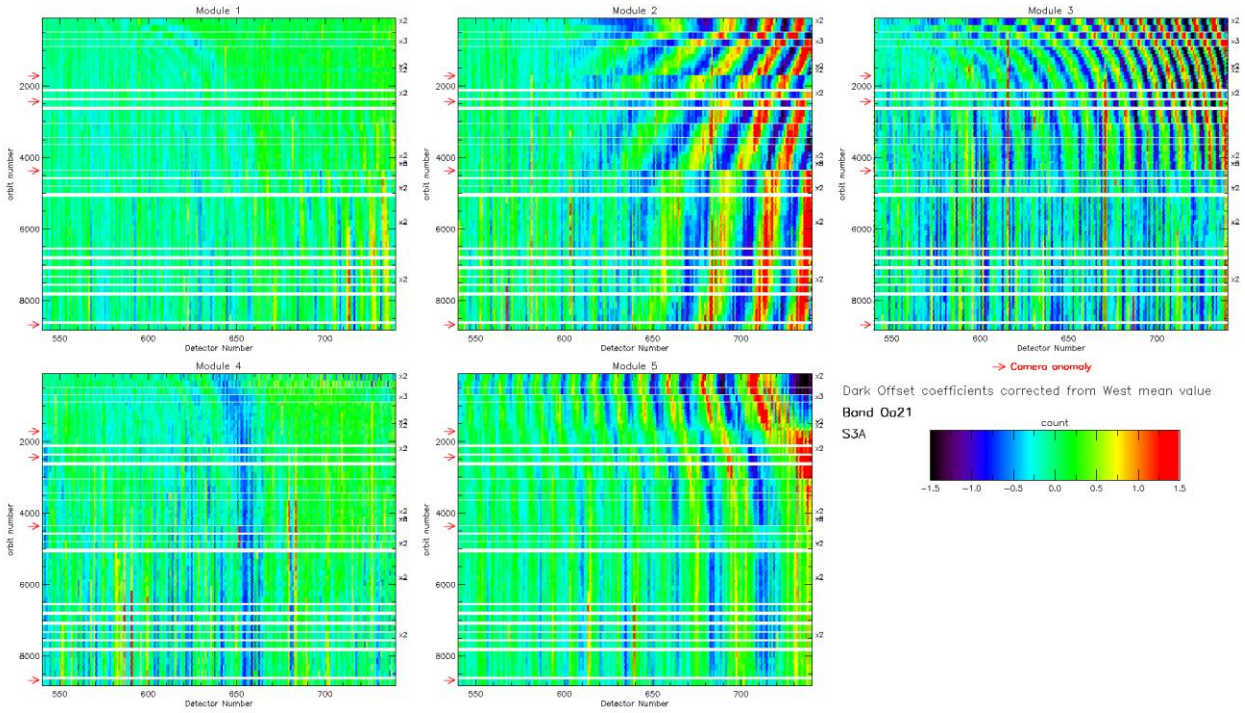

Figure 7: map of periodic noise for the 5 cameras, for band Oa21. X-axis is detector number (East part, from 540 to 740, where the periodic noise occurs), Y-axis is the orbit number. The counts have been corrected from the west detectors mean value (not affected by periodic noise) in order to remove mean level gaps and consequently to have a better visualisation of the long term evolution of the periodic noise structure. Periodic noise amplitude is high in camera 2, 3 and 4. It is lower in camera 4 and small in camera 1.

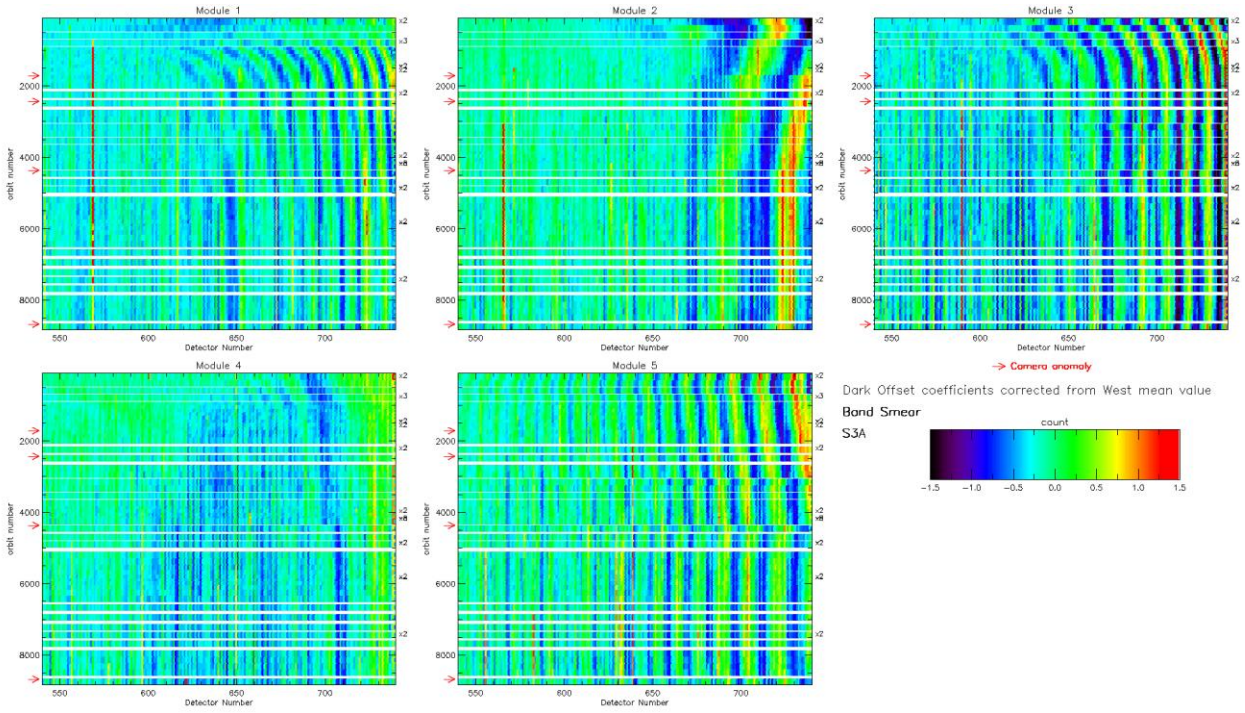

Figure 8: same as Figure 7 for smear band.

Figure 7 and Figure 8 show the so-called 'map of periodic noise' in the 5 cameras, for respectively band 21 and smear band. These maps have been computed from the dark offsets after removal of the mean level of the WEST detectors (not impacted by PN) in order to remove mean level gaps and consequently to highlight the shape of the PN. Maps are focused on the last 200 EAST detectors where PN occurs. We see that the reset of the OLCI instrument performed on 16 OCT 2017, orbit 8666 (following a camera anomaly), had a significant impact on the shape of the PN. The most impacted band is the smear band for camera 5 (see also Figure 9), as well as, to a lesser extent, camera 2 and 3. In band Oa21, the reset of the instrument did not seem to have a significant impact on the shape of the PN even though we can notice that the phase of the PN of camera 2 keeps on drifting since several calibrations.

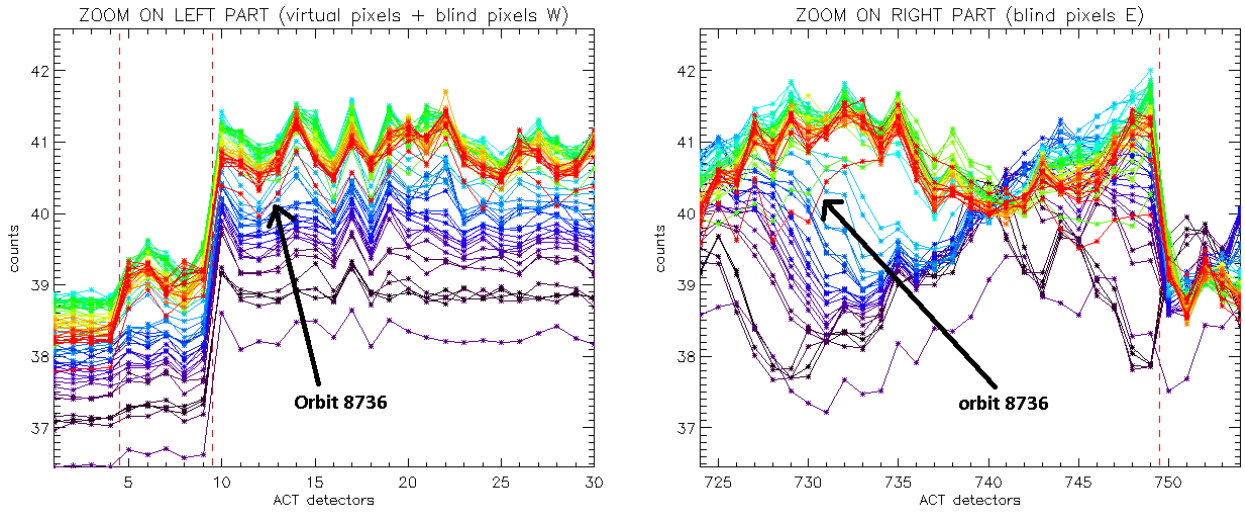

Figure 9: Dark Offset levels for smear band camera 5, for (left plot) first 30 WEST detectors including virtual and blind pixels, (right plot) last 30 EAST detectors including blind pixels. The color of the curves is linked to the orbit number, from the beginning of the mission in black, to the last CALs in red. We see on the right plot that the shape of the PN for the very last CAL (orbit 8736) has been strongly modified by the reset of the OLCI instrument of orbit 8666.As a consequence, the global mean level of the dark offset is impacted by this change of PN, through the OCL convergence, as illustrated in the left plot.

Based on the results presented in Figure 8 and Figure 9, we recommend that the CAL_AX used in PDGS is updated, as soon as possible, with a dark offset table and a dark current table computed from a Calibration sequence posterior to the october2017-anomaly.

Dark Currents

Dark Currents are not affected by the global offset of the Dark Offsets, thanks to the clamping to the average blind pixels value. However, the oscillations of Periodic Noise remain visible. There is no significant evolution of this parameter during the current cycle.

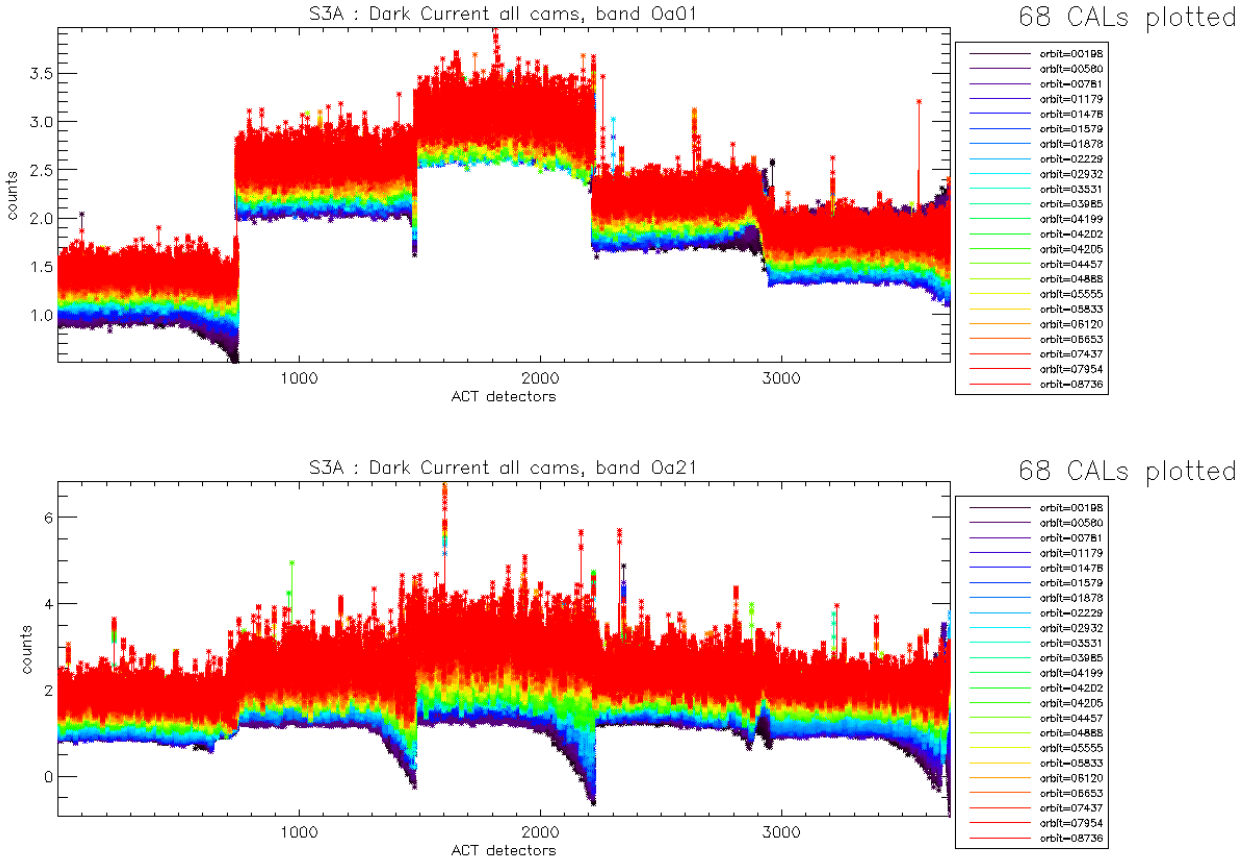

Figure 10: Dark Current for band Oa1 (top) and Oa21 (bottom), all radiometric calibrations so far except the first one (orbit 183) for which the instrument was not thermally stable yet.

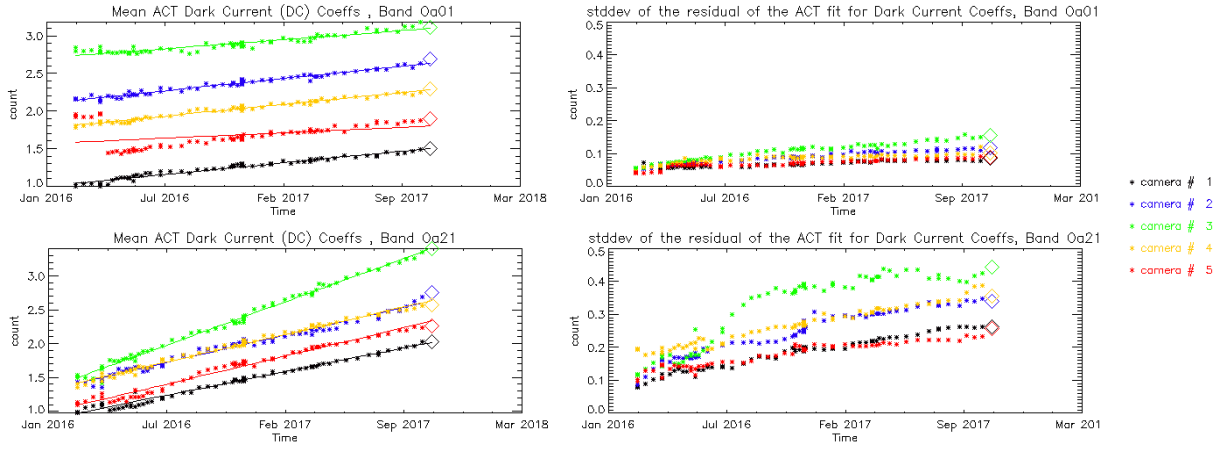

Figure 11: left column: ACT mean on 400 first detectors of Dark Current coefficients for spectral band Oa01 (top) and Oa21 (bottom). Right column: same as left column but for Standard deviation instead of mean. We see an increase of the DC level as a function of time especially for band Oa21. A possible explanation could be the increase of the number of hot pixels which is more important in Oa21 because this band is made of more CCD lines than band Oa01 and thus receives more cosmic rays impacts. It is known that cosmic rays degrade the structure of the CCD, generating more and more hot pixels at long term scales.

1.2.2 Instrument response and degradation modelling [OLCI-L1B-CV-250]

1.2.2.1 Instrument response monitoring

Figure 12 below shows the gain coefficients of every pixel for two OLCI channels, Oa1 (400 nm) and Oa21 (1020 nm), highlighting the significant evolution of the instrument response since early mission.

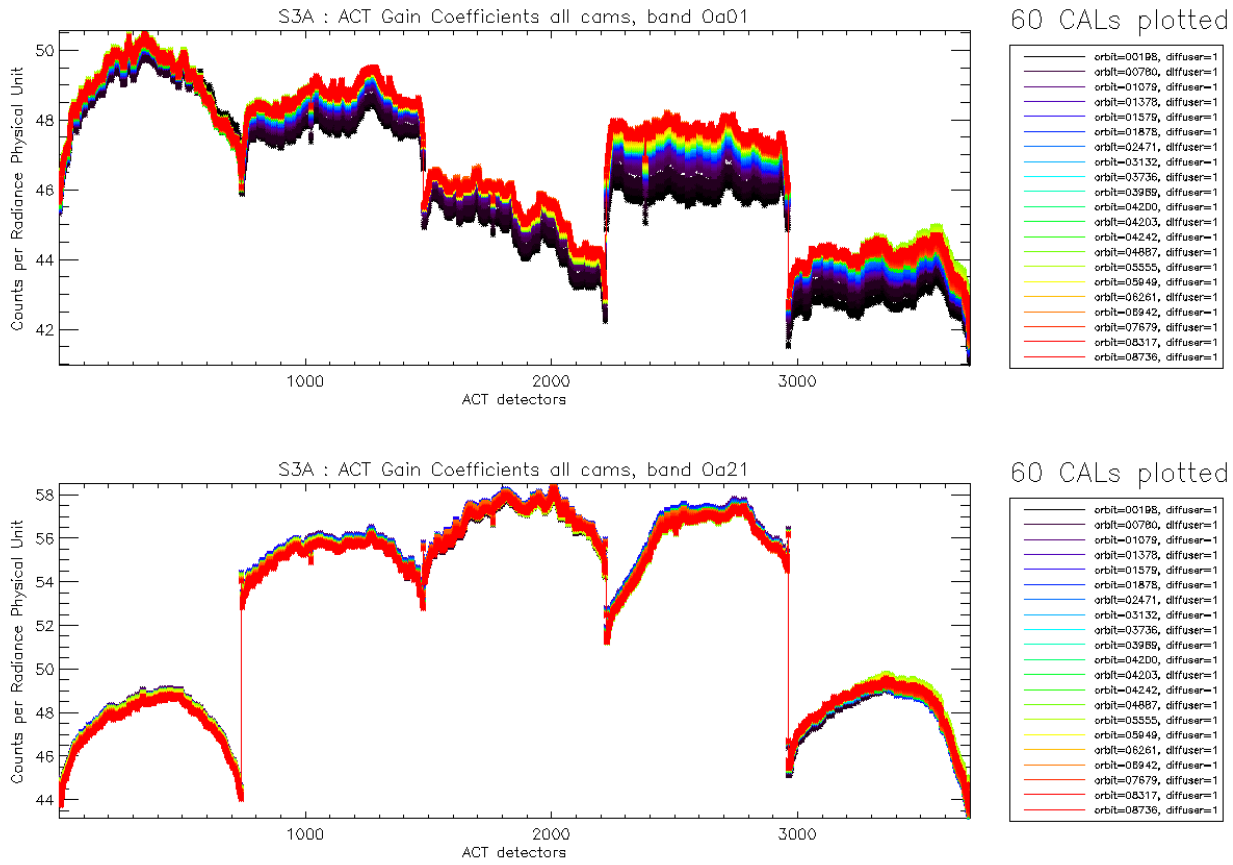

Figure 12: Gain Coefficients for band Oa1 (top) and Oa21 (bottom), all diffuser 1 radiometric calibrations so far except the first one (orbit 183) for which the instrument was not thermally stable yet.

The gains plotted in Figure 12, however are derived using the ground BRDF model – as the only one available in the operational processing software so far – which is known to suffer from illumination geometry dependent residual errors (see previous Cyclic Reports for more details). Consequently they are post-processed to replace the ground BRDF model by the in-flight version, based on Yaw Manoeuvres data, prior to determine the radiometric evolution.

Figure 13 displays a summary of the time evolution derived from post-processed gains: the cross-track average of the BRDF corrected gains is plotted as a function of time, for each module, relative to a given reference calibration (the 12/12/2016). It shows that, if a significant evolution occurred during the early mission, the trends tend to stabilize, with the exception of band 1 of camera 4.

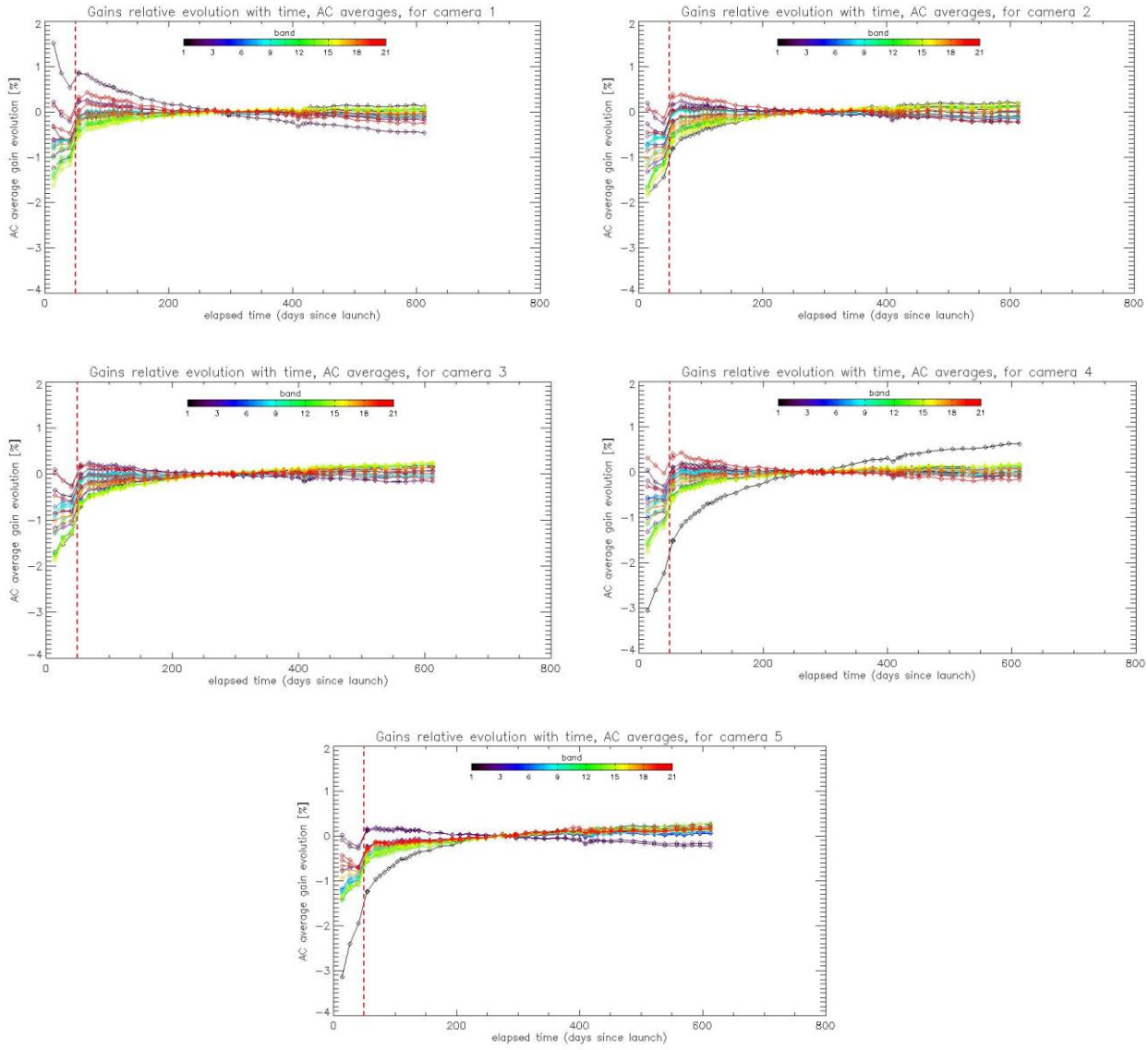

Figure 13: camera averaged gain relative evolution with respect to "best geometry" calibration (22/11/2016), as a function of elapsed time since launch; one curve for each band (see colour code on plots), one plot for each module. The star tracker anomaly fix (6/04/16) is represented by a vertical red dashed line.

The behaviour over the first two months of mission, really different and highlighted by Figure 13, is explained by the Star Tracker software anomaly during which the attitude information provided by the platform was corrupted, preventing to compute a correct illumination geometry, with a significant impact on the gain computation.

1.2.2.2 Instrument evolution modelling

As mentioned in previous Report (cycle 22) the OLCI Radiometric Model has been refreshed, and put in operations the 11/10/2017. The model has been derived on the basis of an extended Radiometric Calibration dataset (from 26/04/2016 to 27/08/2017), and includes the correction of the diffuser ageing for the five bluest bands (Oa1 to Oa5) for which it is clearly measurable. The model performance over

the complete dataset (including the 4 calibrations in extrapolation over two months) remains better than 0.1% when averaged over the whole field of view (Figure 14), while the previous model, trained on a Radiometric Dataset limited to 12/03/2017, shows a slow drift of the model with respect to most recent data (Figure 15). Comparison of the two figures shows the improvement brought by the updated Model.

The overall instrument evolution since channel programming change (25/04/2016) is shown on Figure 14.

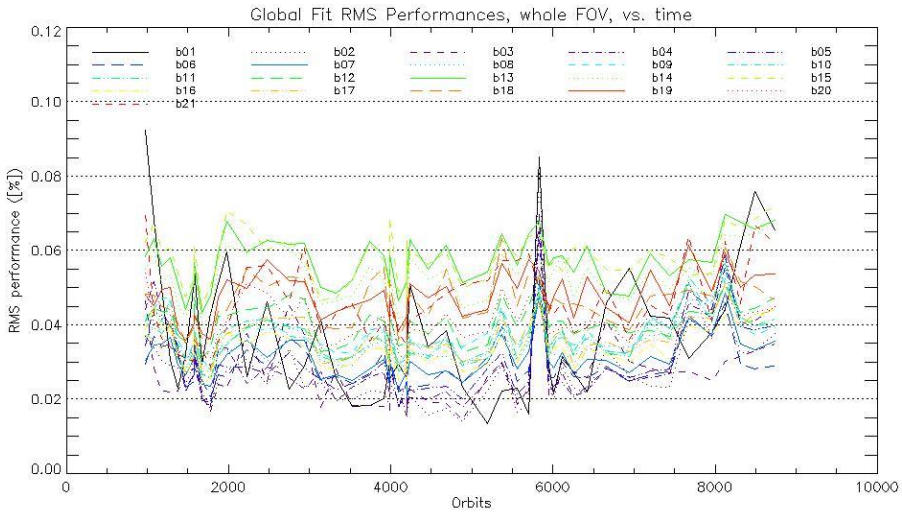

Figure 14: RMS performance of the Gain Model of current Processing Baseline as a function of orbit.

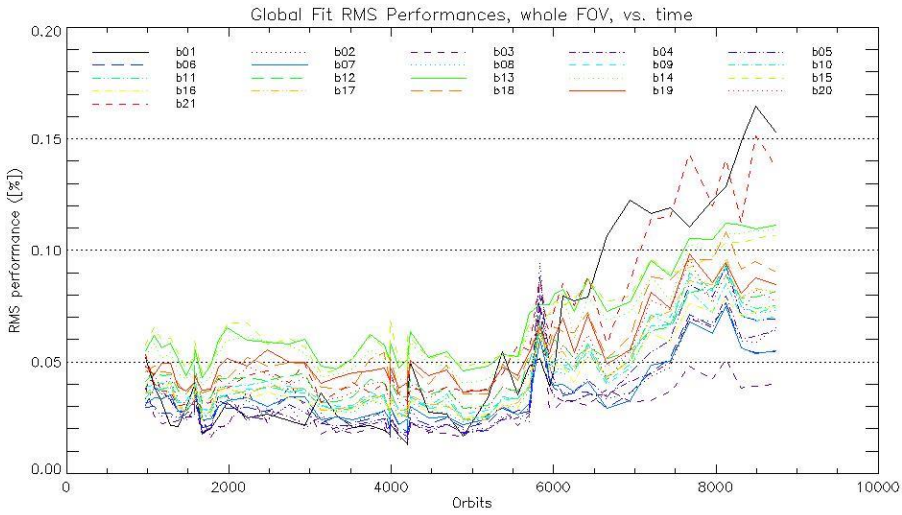

Figure 15: RMS performance of the Gain Model of previous Processing Baseline as a function of orbit.

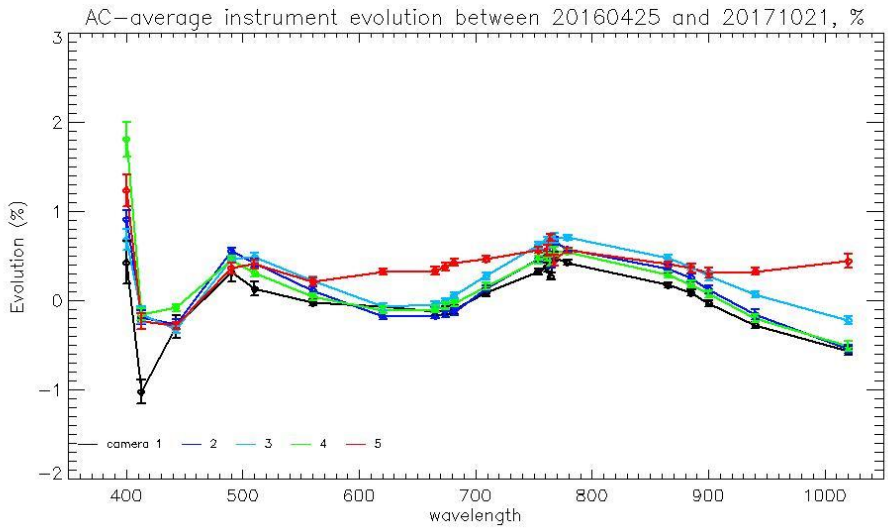

Figure 16: Camera-averaged instrument evolution since channel programming change (25/04/2016) and up to most recent calibration (21/10/2017) versus wavelength.

The overall per camera performance, as a function of wavelength, and at each orbit is shown on Figure 17 as the average and standard deviation of the model over data ratio.

Finally, Figure 18 to Figure 20 show the detail of the model performance, with across-track plots of the model over data ratios at each orbit, one plot for each channel.

Comparisons of Figure 17 to Figure 20 with their counterparts in Report of Cycle 22 clearly demonstrate the improvement brought by the new model whatever the level of detail.

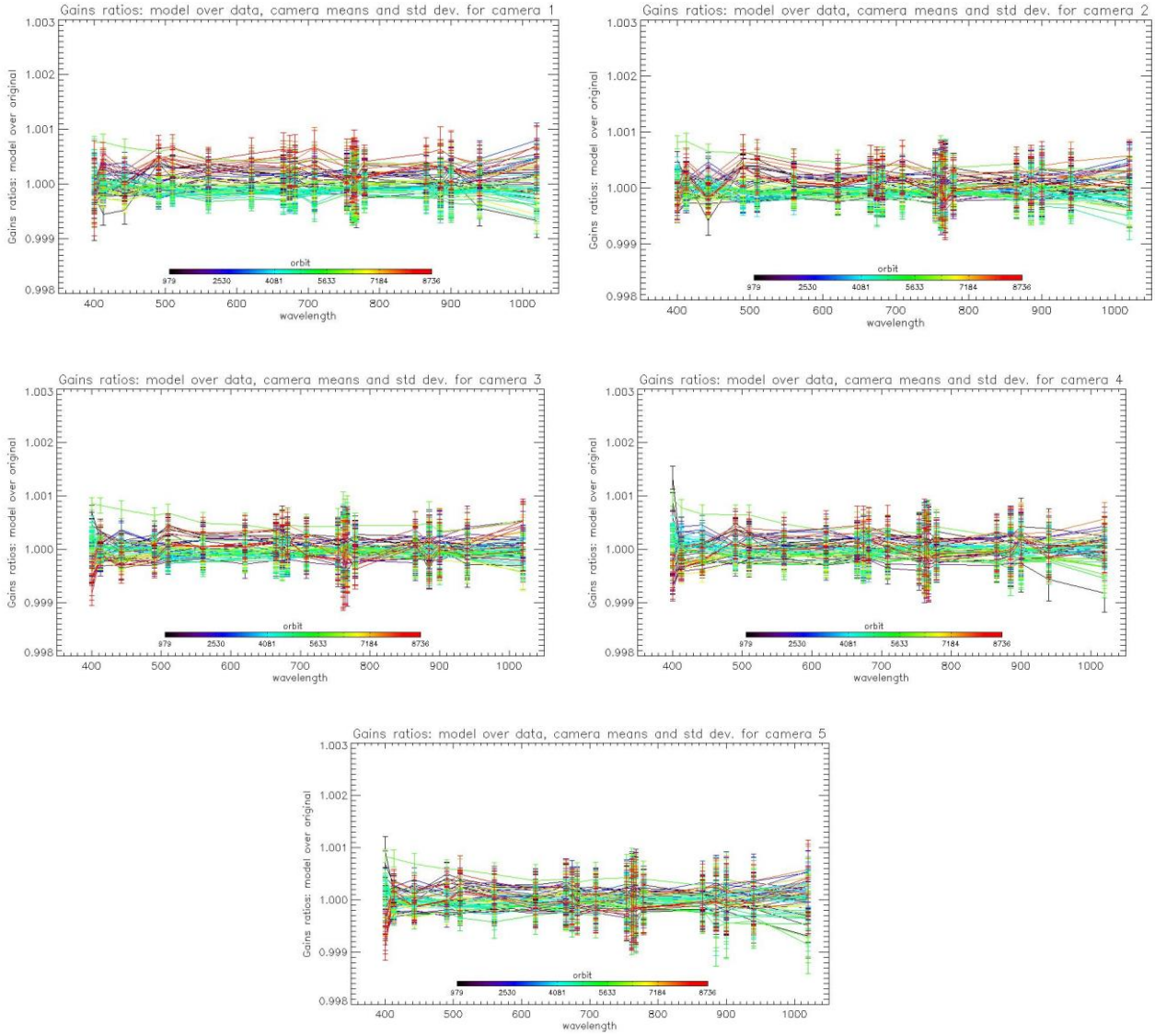

Figure 17: For the 5 cameras: Evolution model performance, as camera-average and standard deviation of ratio of Model over Data vs. wavelength, for each orbit of the test dataset, including 4 calibration in extrapolation, with a colour code for each calibration from blue (oldest) to red (most recent).

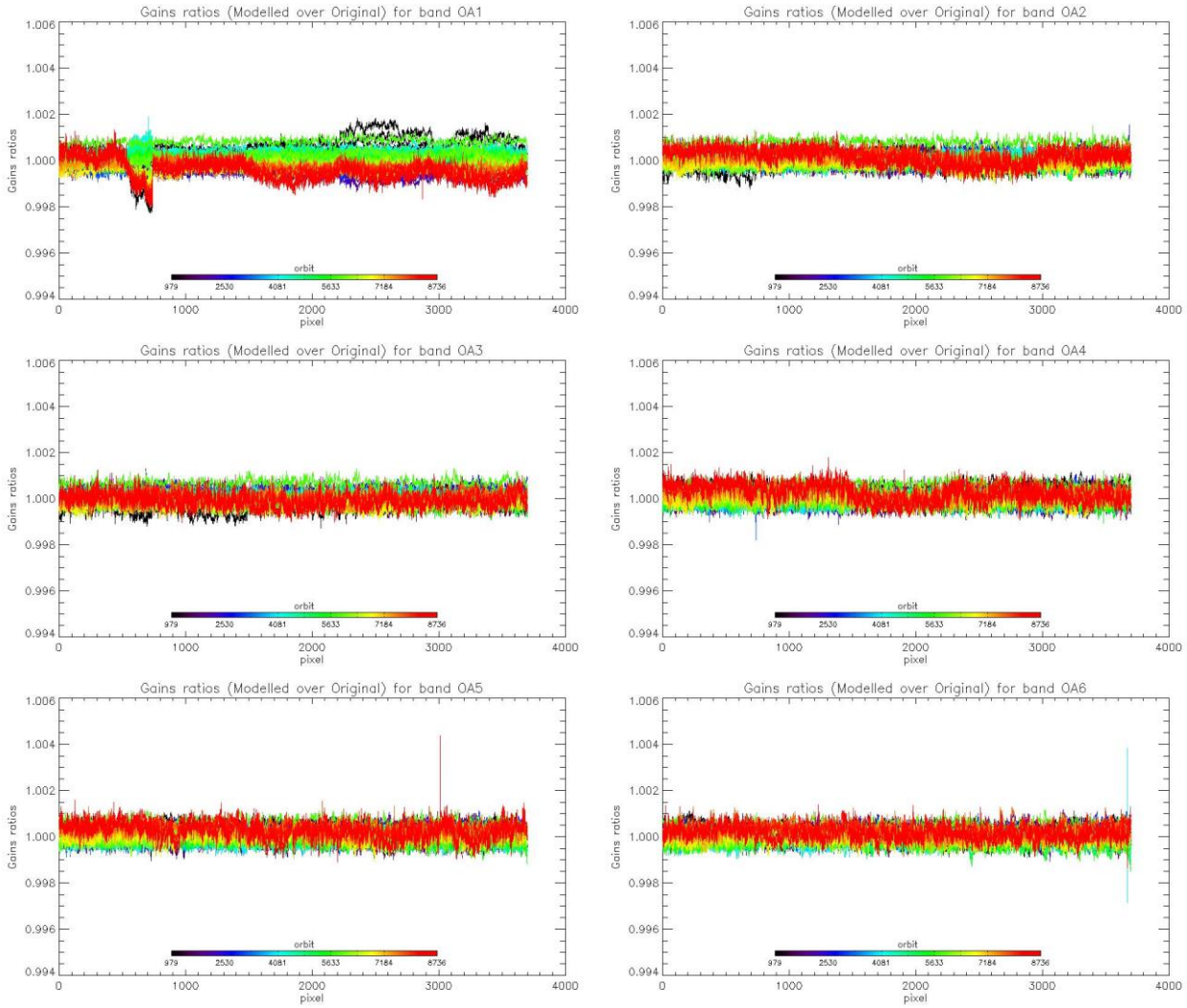

Figure 18: Evolution model performance, as ratio of Model over Data vs. pixels, all cameras side by side, over the whole current calibration dataset (since instrument programing update), including 4 calibrations in extrapolation, channels Oa1 to Oa6.

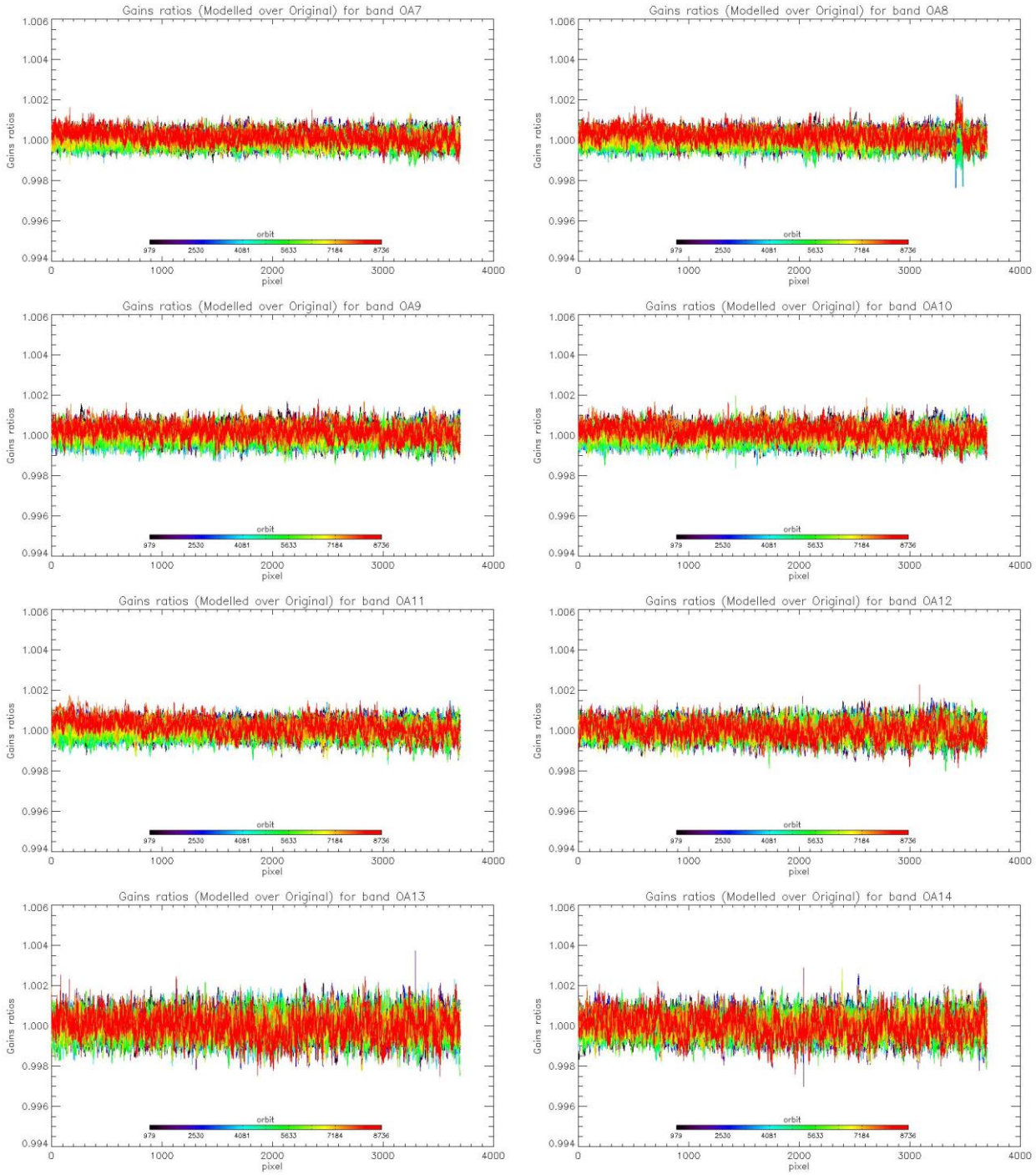

Figure 19: same as Figure 14 for channels Oa7 to Oa14.

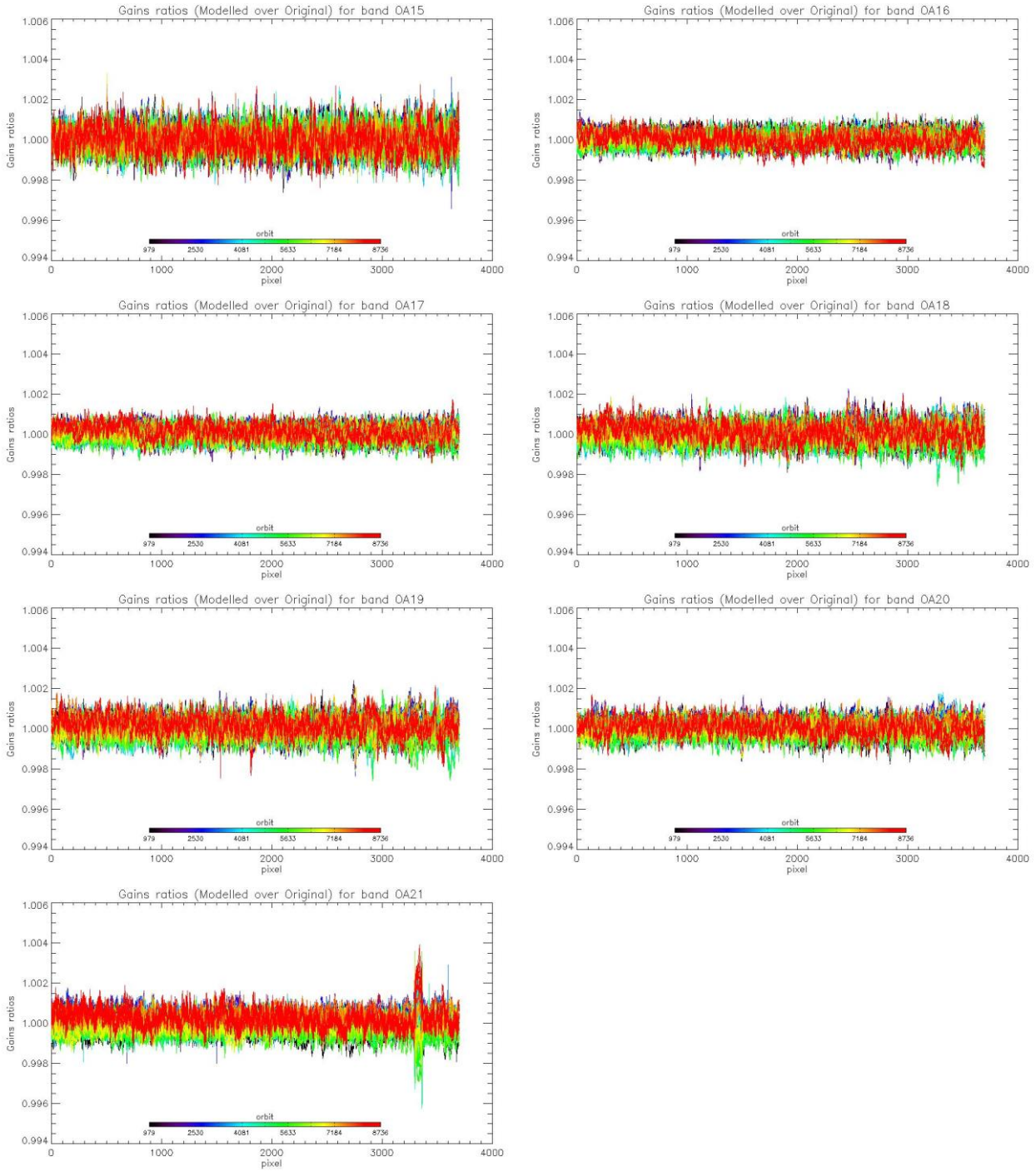

Figure 20: same as Figure 18 for channels Oa15 to Oa21.

1.2.3 Ageing of nominal diffuser [OLCI-L1B-CV-240]

There has been no calibration sequence S05 (reference diffuser) acquisition during cycle 023.

Consequently the last updated results (cycle 020) are still valid.

On the other hand, results of Cycle 020 have been used to derive a model of diffuser ageing as a function of cumulated exposure time (i.e. number of acquisition sequence on nominal diffuser, regardless of the band setting). This model has in turn been used to derive a new Gain Model, recently put in operations (11/10/2017). A dedicated Verification Report has been issued (S3MPC.ACR.VR.025).

The results of the ageing modelling are shortly summarised and illustrated here. Figure 21 confirms the need to model ageing against cumulated exposure rather than elapsed time, as it provides a more linear trend, even if not perfect. It is likely that BRDF effects are not totally screened out. Figure 22 show the non-linear relationship between cumulated exposure and time.

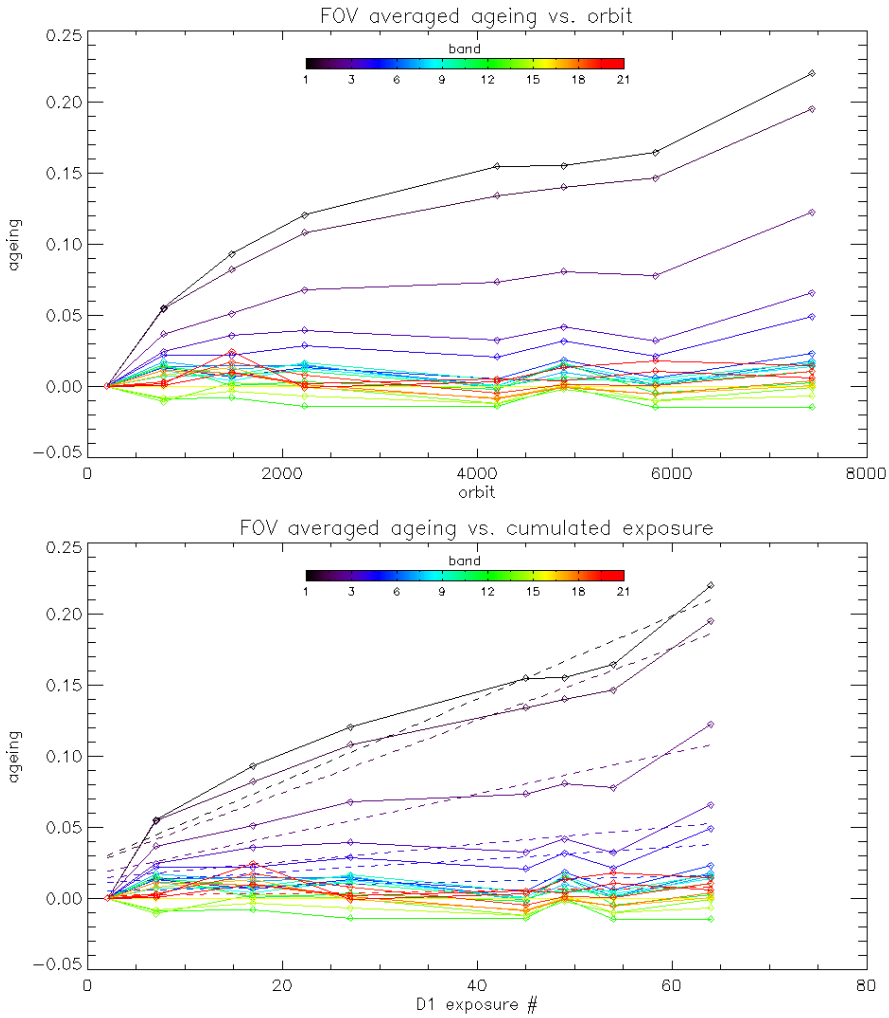

Figure 21 : FOV-averaged ageing for each band (see colour code) vs time (top) and cumulated exposures (bottom).

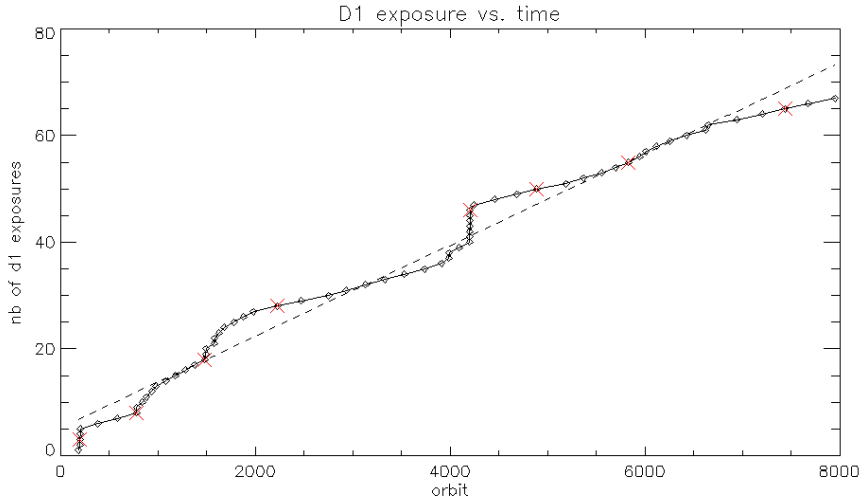

Figure 22 : cumulated exposure versus time (absolute orbit). The steep slope around orbit 4200 corresponds to the Yaw Manoeuvres.

Figure 23 summarises the fit results and some of the correction criteria. The black curve is the slope of the linear fit, scaled to 100 exposures (i.e. about 2 years at nominal acquisition rate) and the green curve is the intercept, both against wavelength. The spectral shape of the slope curve, as well as its magnitude fits correctly with expectations based on MERIS experience. Intercepts are small enough to be ignored. The red curve is the correlation coefficient, one of the criteria to decide whether a correction is reliable enough to be applied; the threshold has been set to 0.5, selecting only the first 6 bands. Another criterion is the total amount of ageing measured so far, set to a minimum 0.02%, additionally eliminates band Oa6.

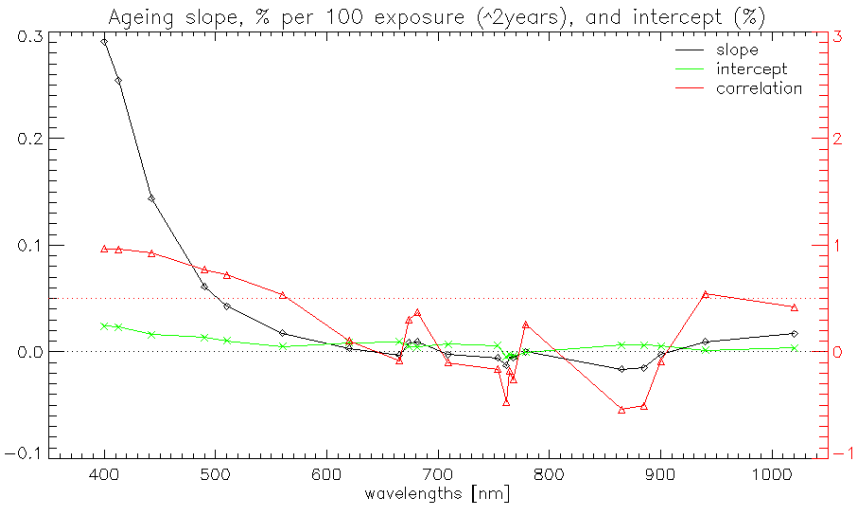

Figure 23 : intercept and slopes of ageing fits (black and green lines respectively, referring to left axis), and correlation coefficients (red, referring to right axis) versus wavelength.

1.2.4 Updating of calibration ADF [OLCI-L1B-CV-260]

A calibration ADF has been generated for the new Processing Baseline. It includes Dark Correction tables with HEP filtering (see above) and the updated Gain Model, accounting for all available RC up to cycle 21 and the ageing of the nominal diffuser (see section 1.2.2).

S3A_OL_1_CAL_AX_20170827T142237_20991231T235959_20170915T120000_____MPC_O_AL_017.SEN3

1.2.5 Radiometric Calibrations for sun azimuth angle dependency and Yaw Manoeuvres for Solar Diffuser on-orbit re-characterization [OLCI-L1B-CV-270 and OLCI-L1B-CV-280]

This activity has not evolved during cycle 023 and results presented in previous report are still valid.

1.3 Spectral Calibration [OLCI-L1B-CV-400]

There has been no Spectral Calibration acquisitions sequence S02/S03 during cycle 023.

Consequently the last updated results (cycle 018) are still valid.

1.4 Signal to Noise assessment [OLCI-L1B-CV-620]

1.4.1 SNR from Radiometric calibration data.

SNR computed for all calibration data as a function of band number is presented in Figure 24.

SNR computed for all calibration data as a function of orbit number for band Oa01 (the less stable band) is presented in Figure 25.

There is no significant evolution of this parameter during the current cycle and the ESA requirement is fulfilled for all bands.

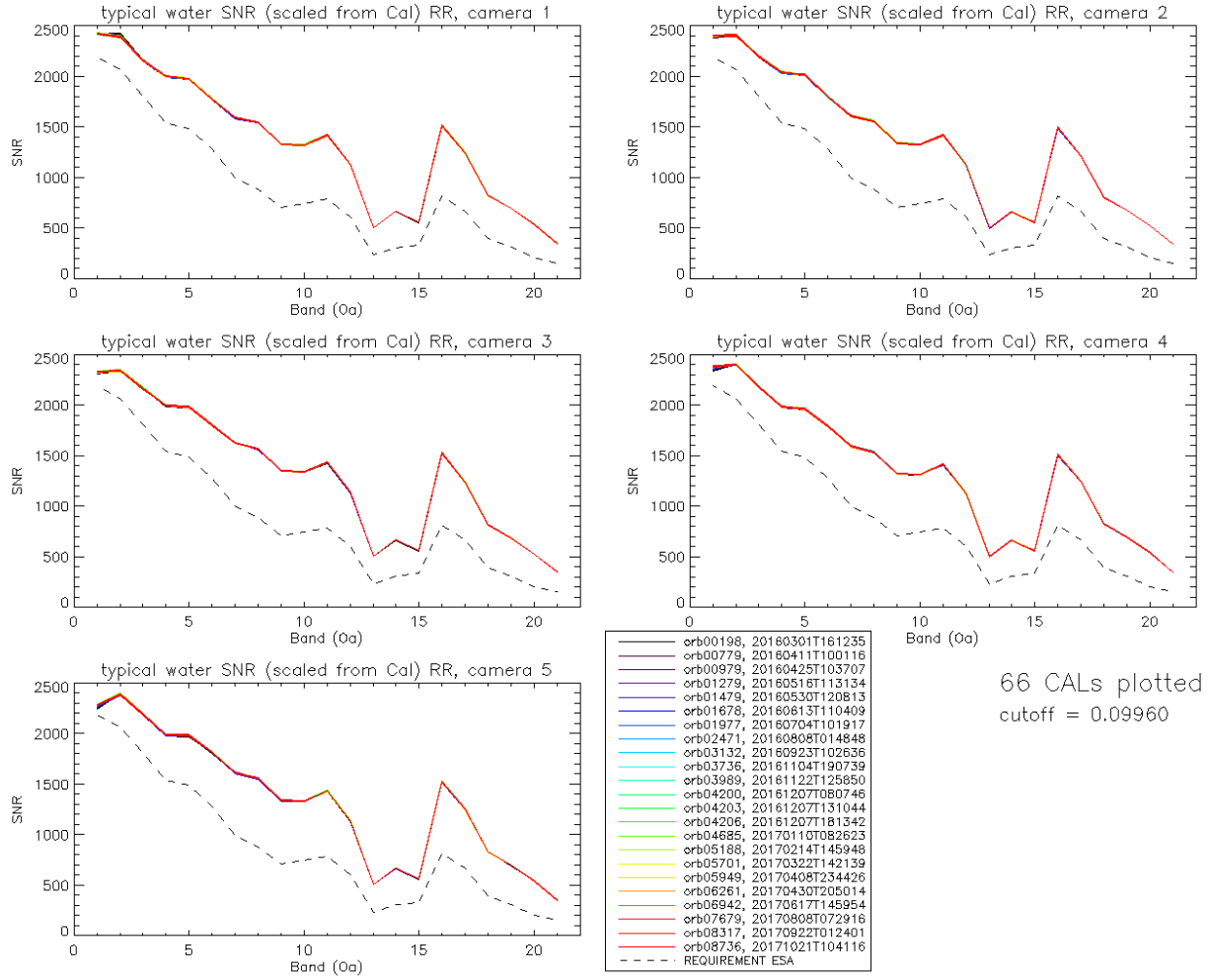

Figure 24: Signal to Noise ratio as a function of the spectral band for the 5 cameras. These results have been computed from radiometric calibration data. All calibrations except first one (orbit 183) are presents with the colours corresponding to the orbit number (see legend). The SNR is very stable with time: the curves for all orbits are almost superimposed. The dashed curve is the ESA requirement.

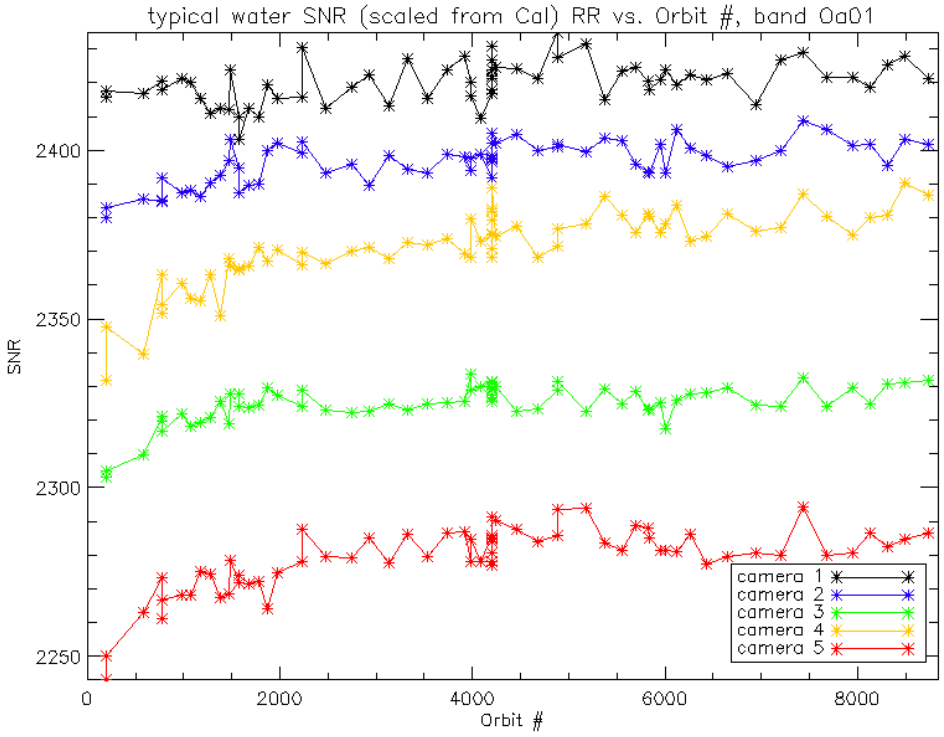

Figure 25: long-term stability of the SNR estimates from Calibration data, example of channel Oa1.

The mission averaged SNR figures are provided in Table 1 below, together with their radiance reference level. According to the OLCI SNR requirements, these figures are valid at these radiance levels and at Reduced Resolution (RR, 1.2 km). They can be scaled to other radiance levels assuming shot noise (CCD sensor noise) is the dominating term, i.e. radiometric noise can be considered Gaussian with its standard deviation varying as the square root of the signal; in other words: $SNR(L) = SNR(L_{ref}) \cdot \sqrt{\frac{L}{L_{ref}}}$. Following the same assumption, values at Full Resolution (300m) can be derived from RR ones as 4 times smaller.

Table 1: SNR figures as derived from Radiometric Calibration data. Figures are given for each camera (time average and standard deviation), and for the whole instrument. The requirement and its reference radiance level are recalled (in $mW.sr^{-1}.m^{-2}.nm^{-1}$).

λ	L_{ref}	SNR	C1		C2		C3		C4		C5		All	
nm	LU	RQT	avg	*std*	avg	*std*	avg	*std*	avg	*std*	avg	*std*	avg	*std*
400	63	2188	2420	6	2396	6.2	2324	5.8	2371	11.2	2279	9.5	2358	6.5
412	74.1	2061	2396	7.6	2409	5.2	2340	4.9	2401	4.4	2386	6.9	2386	3.9
442	65.6	1811	2161	5.3	2199	5.7	2166	4.6	2185	4.2	2197	4.9	2182	3.3
490	51.2	1541	1999	5	2035	5.3	1995	3.5	1981	4.1	1987	5	2000	3.5
510	44.4	1488	1979	5.4	2013	4.9	1983	4.6	1965	4.4	1984	4.9	1985	3.8
560	31.5	1280	1775	4.3	1801	4.3	1801	4.8	1793	4	1817	3.7	1798	3.2
620	21.1	997	1591	4.1	1609	4.2	1625	3.2	1593	3.5	1614	3.5	1606	2.7
665	16.4	883	1546	4.6	1558	4.1	1566	3.8	1533	3.9	1560	3.8	1552	3.2
674	15.7	707	1329	3.4	1338	3.8	1350	2.9	1323	3.1	1341	3.8	1336	2.6
681	15.1	745	1319	3.7	1326	3.1	1337	2.9	1314	2.5	1332	3.7	1326	2.2
709	12.7	785	1420	4.6	1420	4.3	1434	3.5	1413	3.7	1429	3	1423	3
754	10.3	605	1127	3.4	1120	3.1	1133	3.4	1123	2.4	1138	2.8	1128	2.5
761	6.1	232	501	1.2	498	1.3	505	1.2	500	1.1	507	1.5	502	1
764	7.1	305	662	1.6	657	1.6	667	2.2	661	1.6	669	2	663	1.5
768	7.6	330	558	1.7	554	1.3	561	1.3	556	1.6	564	1.3	558	1.2
779	9.2	812	1514	5.2	1496	5.1	1523	5.5	1509	5.4	1524	5	1513	4.6
865	6.2	666	1243	3.8	1212	4.4	1237	4.3	1245	3.9	1249	3	1237	3.3
885	6	395	823	1.9	801	1.7	813	2	824	1.5	831	1.8	818	1.3
900	4.7	308	691	1.5	673	1.3	683	1.8	693	1.5	698	1.5	687	1.1
940	2.4	203	534	1.1	522	1.1	525	1	539	1.2	542	1.3	532	0.8
1020	3.9	152	345	0.8	337	0.7	348	0.8	345	0.7	351	0.7	345	0.5

1.4.2 SNR from EO data.

There has been no update on SNR assessment from EO data during the cycle. Last figures (cycle 9) are considered valid.

1.5 Geometric Calibration/Validation

Regular monitoring using the GeoCal Tool implemented within the MPMF continues. Late August results confirm good performance. Monitoring of the geolocation performance by correlation with GCP imagettes using the GeoCal tool over the period confirms that OLCI is compliant with its requirement: the centroid of the geolocation error is around 0.25 to 0.35 pixel in both along-track and across-track directions (Figure 26 & Figure 27). The dispersion of the along-track errors in Figure 27 suggests however that a per-camera analysis is required, it is on-going. Completion of the time series (started using the partial reprocessing dedicated to validation: 4 days every month between 26/04/16 and 12/03/2017) confirms the slow AL trend (Figure 28).

Performing additional geometric Calibration has to be done in a near future. The required complete version of the GeoCal tool, allowing the Calibration mode, has recently been installed in the MPMF and Geometric Calibration will start as soon as possible.

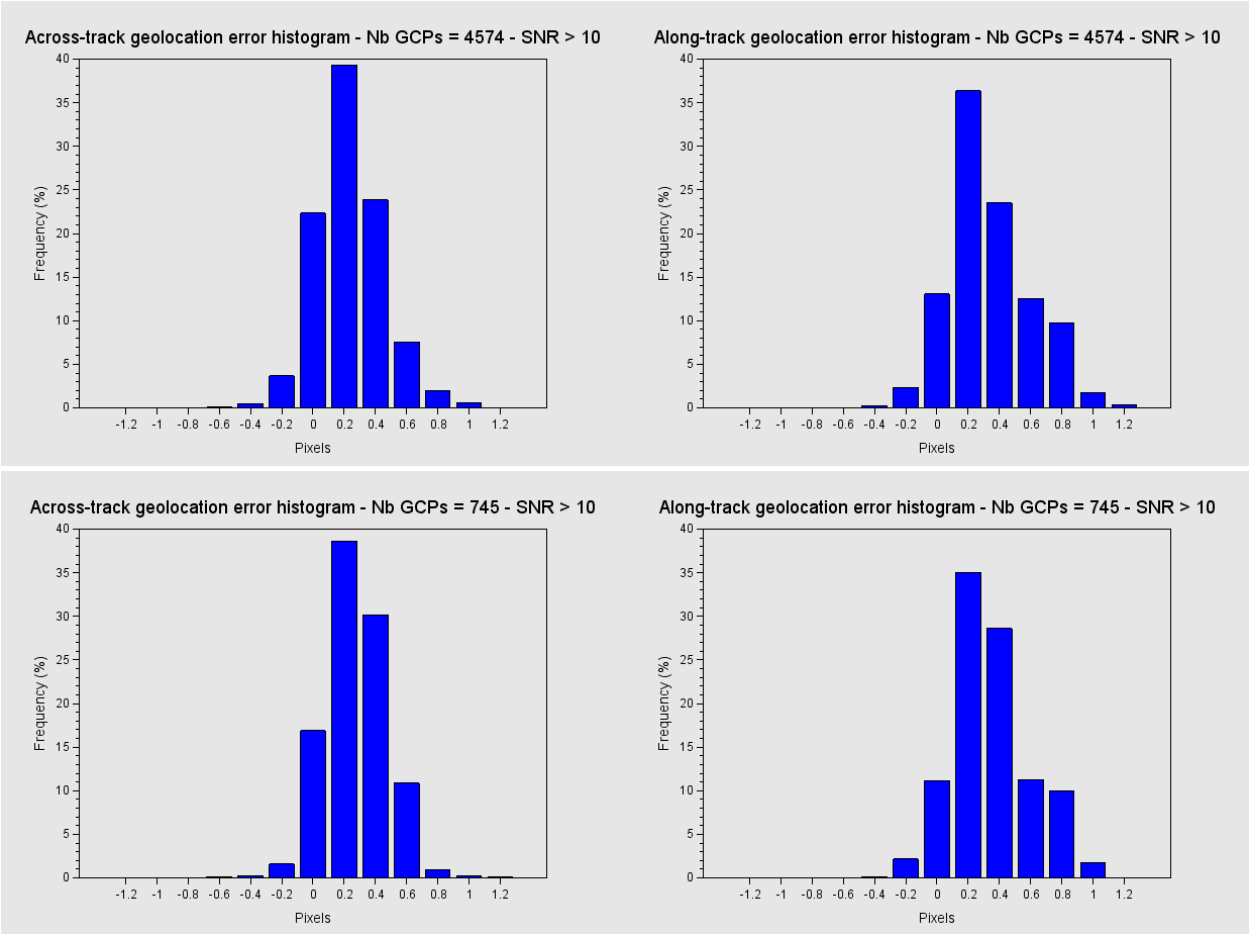

Figure 26: histograms of geolocation errors for the along-track (left) and across-track (right) directions, examples of 01/10/2017 (top) and 26/10/2017 (bottom).

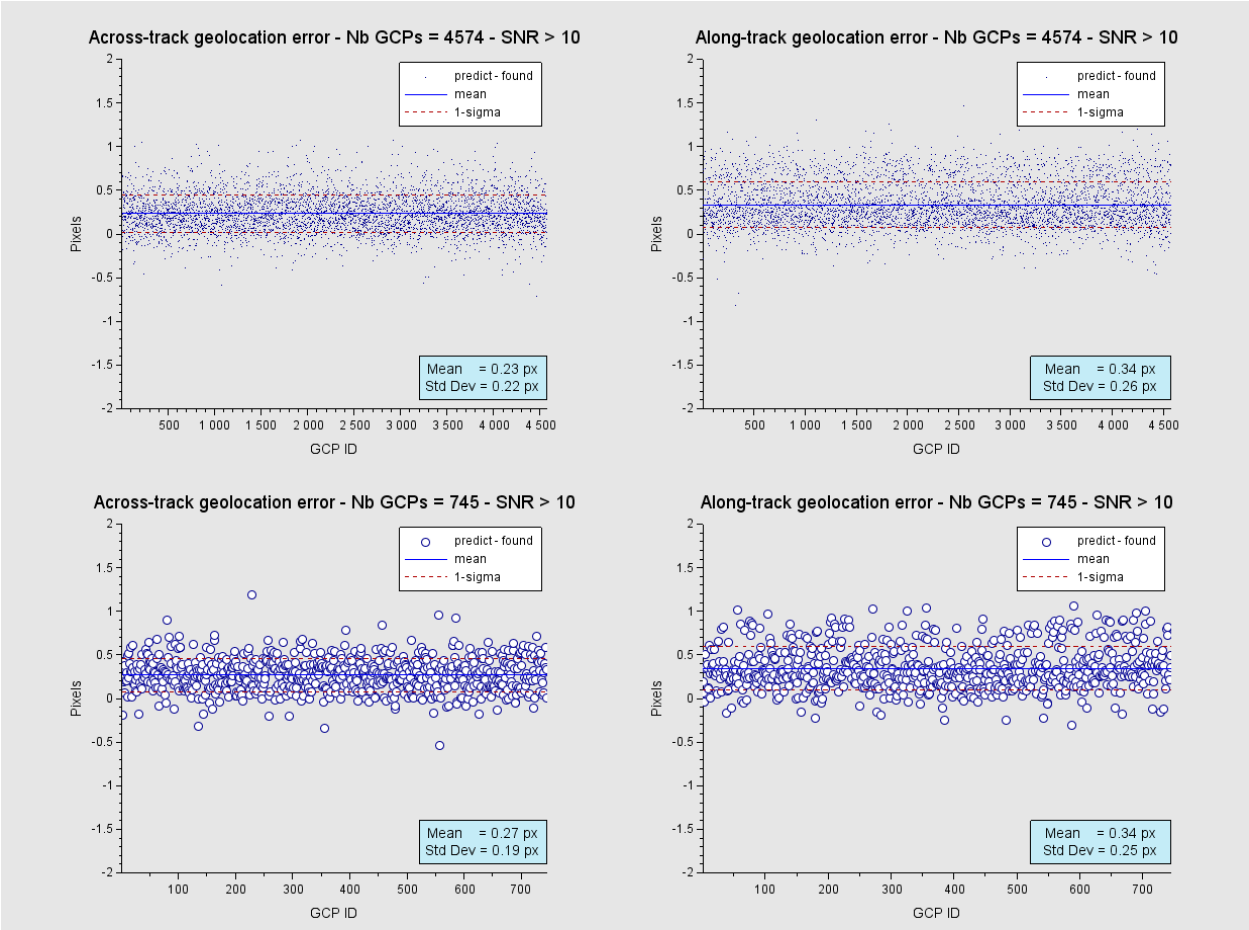

Figure 27: georeferencing error in along-track (left) and across-track (right) directions for all the GCPs, examples of 01/10/2017 (top) and 26/10/2017 (bottom). Note that the symbol size in bottom figure is linked to the lower number of GCPs.

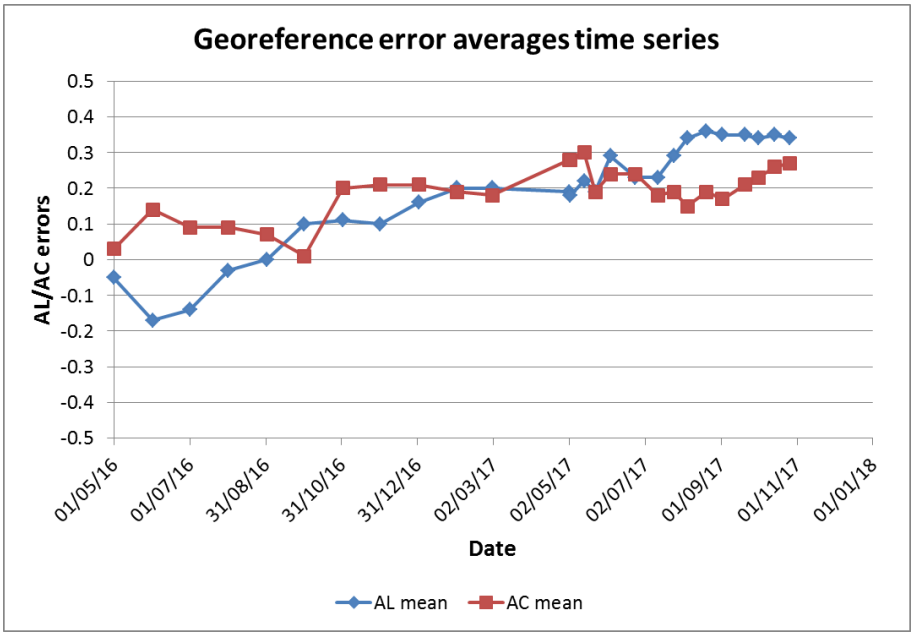

Figure 28: time series of geolocation errors for the along-track (blue) and across-track (red) directions over 15.6 months.

2 OLCI Level 1 Product validation

2.1 [OLCI-L1B-CV-300], [OLCI-L1B-CV-310] – Radiometric Validation

2.1.1 S3ETRAC Service

Activities done

The S3ETRAC service extracts OLCI L1 RR and SLSTR L1 RBT data and computes associated statistics over 49 sites corresponding to different surface types (desert, snow, ocean maximizing Rayleigh signal, ocean maximizing sunglint scattering and deep convective clouds). The S3ETRAC products are used for the assessment and monitoring of the L1 radiometry (optical channels) by the ESLs.

All details about the S3ETRAC/OLCI and S3ETRAC/SLSTR statistics are provided on the S3ETRAC website http://s3etrac.acri.fr/index.php?action=generalstatistics

- Number of OLCI products processed by the S3ETRAC service
- Statistics per type of target (DESERT, SNOW, RAYLEIGH, SUNGLINT and DCC)
- Statistics per sites
- Statistics on the number of records

For illustration, we provide below statistics on the number of S3ETRAC/OLCI records generated per type of targets (DESERT, SNOW, RAYLEIGH, SUNGLINT and DCC).

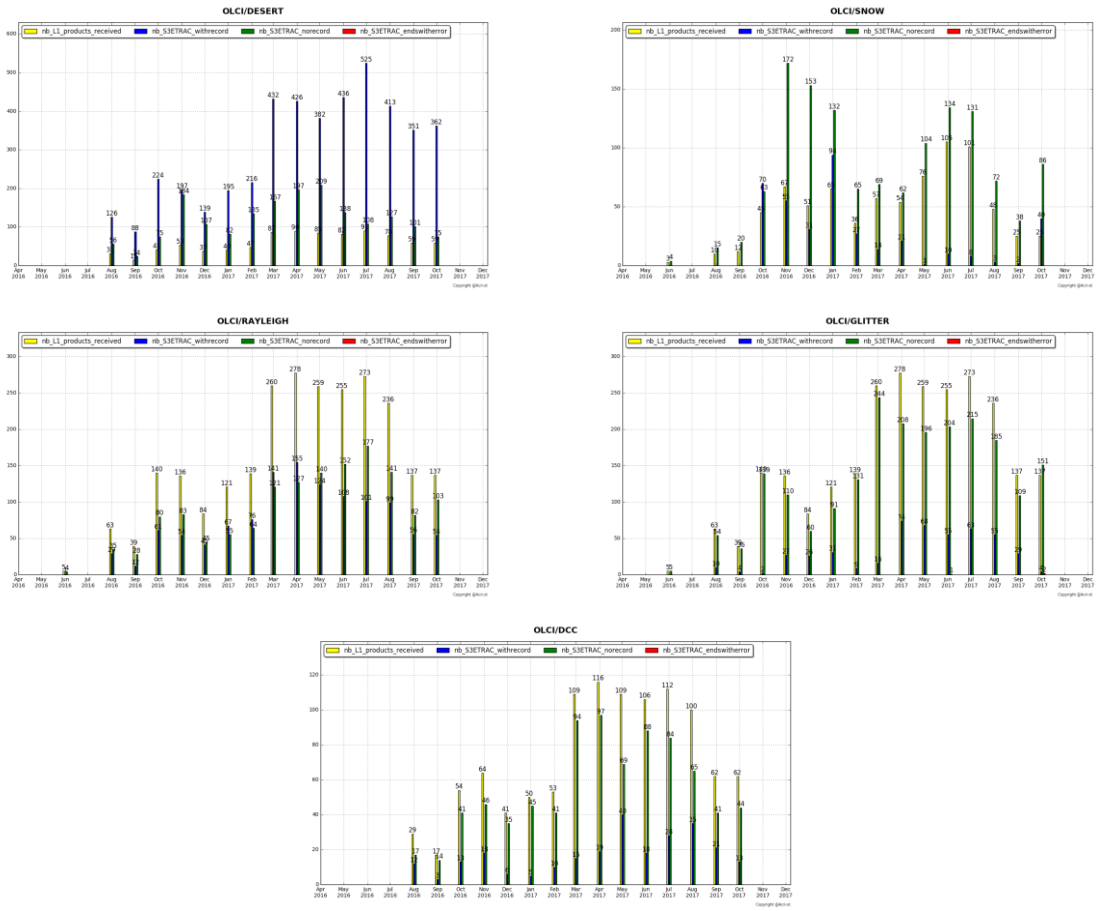

Figure 29: summary of S3ETRAC products generation for OLCI (number of OLCI L1 products Ingested, yellow – number of S3ETRAC extracted products generated, blue – number of S3ETRAC runs without generation of output product (data not meeting selection requirements), green – number of runs ending in error, red, one plot per site type).

2.1.2 Radiometric validation with DIMITRI

Highlights

- Run Rayleigh and Glint methods over the available products until 27th October 2017.
- Run Desert method over the available products until 27th October 2017.
- About 38 new products from Cycle-23 were used in this analysis. The results (Rayleigh, Glint and PICS) are consistent with the previous cycle over the used CalVal sites.
- Good stability of the sensor could be observed, nevertheless, the time-series average shows higher reflectance over the VNIR spectral range with biases of 3%-5% except bands Oa06-Oa09
- Bands with high gaseous absorption are excluded.
- The results need to be consolidated over ocean sites with more products from early mission period (before Dec 2016)..

I-Validation over PICS

1. Downloading and ingestion of all the available L1B-LN1-NT products in the S3A-Opt database over the 6 desert CalVal-sites (Algeria3 & 5, Libya 1 & 4 and Mauritania 1 & 2) has been performed until 27th October 2017.

2. The results are consistent overall the six used PICS sites (Figure 30). OLCI reflectance shows a good stability over the mission life-time.

3. The temporal average over the period **April 2016 – October 2017** of the elementary ratios (observed reflectance to the simulated one) shows values higher than 2% (mission requirements) over all the VNIR bands (Figure 31). The spectral bands with significant absorption from water vapour and O_2 (Oa11, Oa13 and Oa14) are excluded.

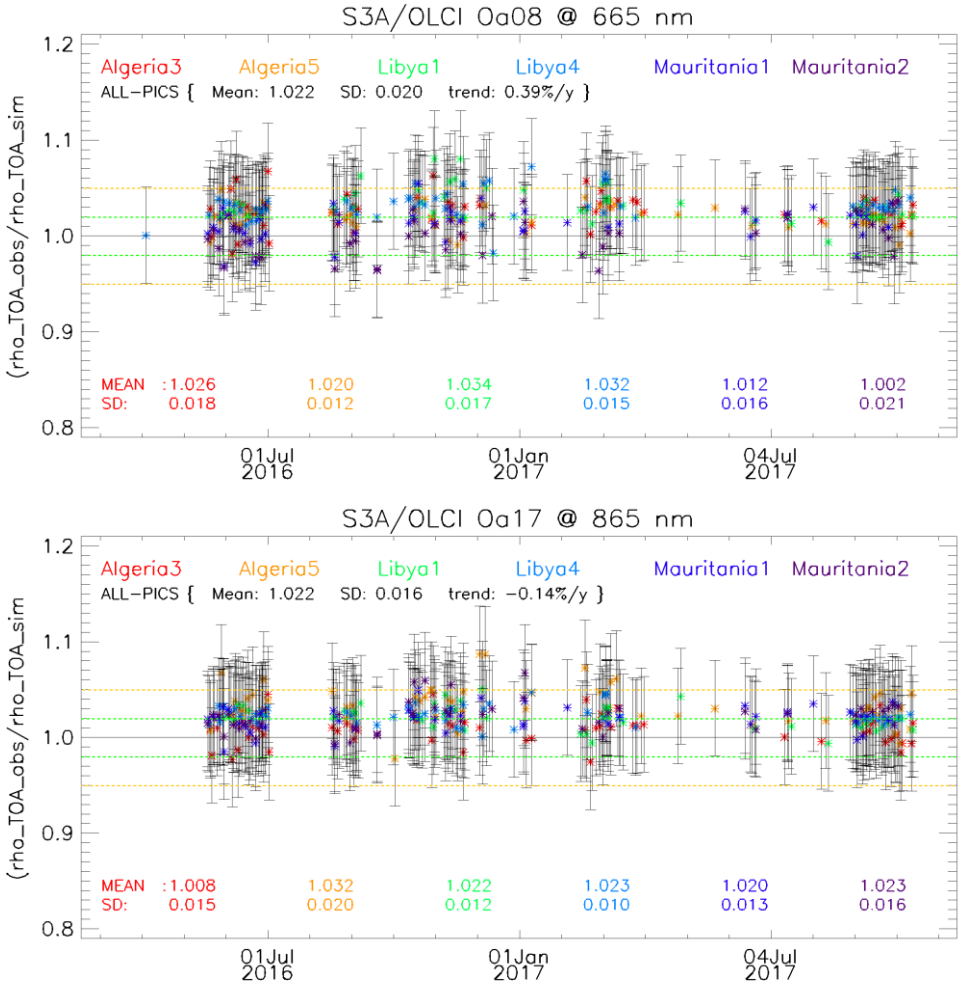

Figure 30: **Time-series of the elementary ratios (observed/simulated) signal from S3A/OLCI for (top to bottom) bands Oa03, Oa8 and Oa17 respectively over Six PICS Cal/Val sites. Dashed-green and orange lines indicate the 2% and 5% respectively. Error bars indicate the desert methodology uncertainty.**

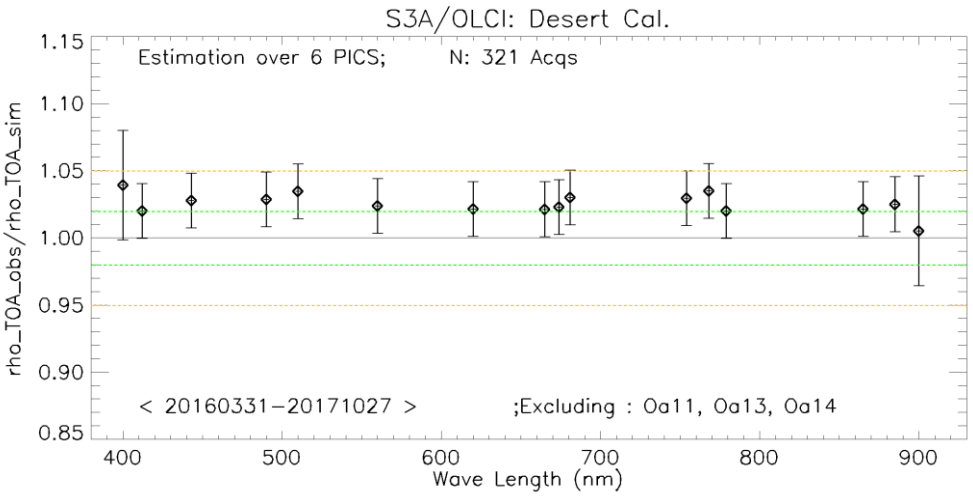

Figure 31: The estimated gain values for S3A/OLCI over the 6 PICS sites identified by CEOS over the period April 2016 – October 2017 as a function of wavelength. Dashed-green and orange lines indicate the 2% and 5% respectively. Error bars indicate the desert methodology uncertainty.

II-Intercomparison S3A/OLCI, S2A/MSI and LANDSAT/OLI over PICS

X-mission Intercomparison with MSI-A and MODIS-A is performed until October 2017. Figure 32 shows time-series of the elementary ratios from S2A/MSI and S3A/OLCI over the LYBIA4 site over the period April-2016 until October-2017.

We observe a clear stability over both sensors, associated with higher reflectance from OLCI wrt to MSI.

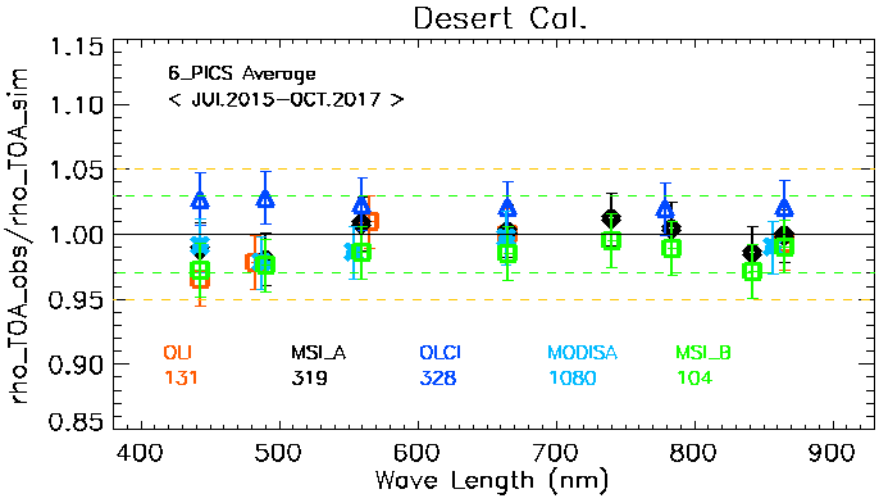

Figure 33 shows the estimated gain over the different time-series from different sensors (MODISA, MSIA, MSIB, OLCI and OLI) over PICS for the common bands with S2A/MSI. The spectral bands with significant absorption from water vapor and O_2 are excluded. Again Figure 31 confirms a systematic higher reflectance of OLCI wrt MSI and MODISA.

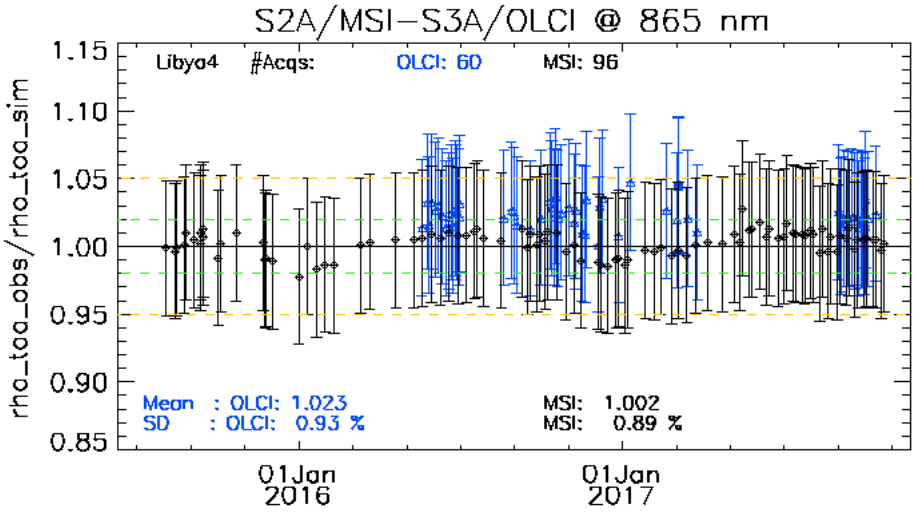

Figure 32: Time-series of the elementary ratios (observed/simulated) signal from (black) S2A/MSI, (blue) S3A/OLCI for band Oa17 (865nm) over the LIBYA4 site. Dashed-green and orange lines indicate the 2% and 5% respectively. Error bars indicate the desert methodology uncertainty.

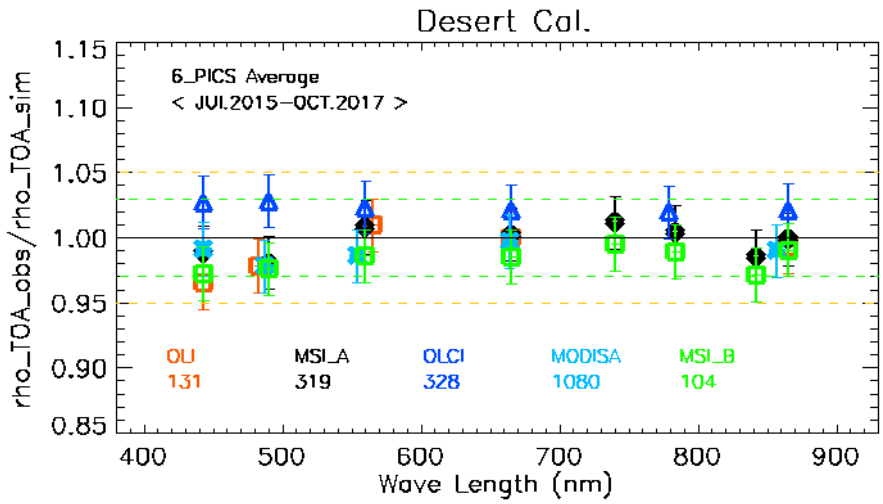

Figure 33: The estimated gain values (observed-signal /simulated-signal) averaged over different period from different sensors over PICS as function of wavelength. The number of used-acquisitions for each sensor within the period July 2015-October 2017 is indicated in the plot-legend.

III-Validation over Rayleigh

Rayleigh method has been performed over the available mini-files on the Opt-server until the cycle-23 period. The results produced with the configuration (ROI-AVERAGE) are consistent with the previous results of PICS method and from Cycles 22. While bands Oa01-Oa05 display a bias values between 2%-5%, bands Oa6-Oa9 exhibit biases within 2% (mission requirements) (Figure 34).

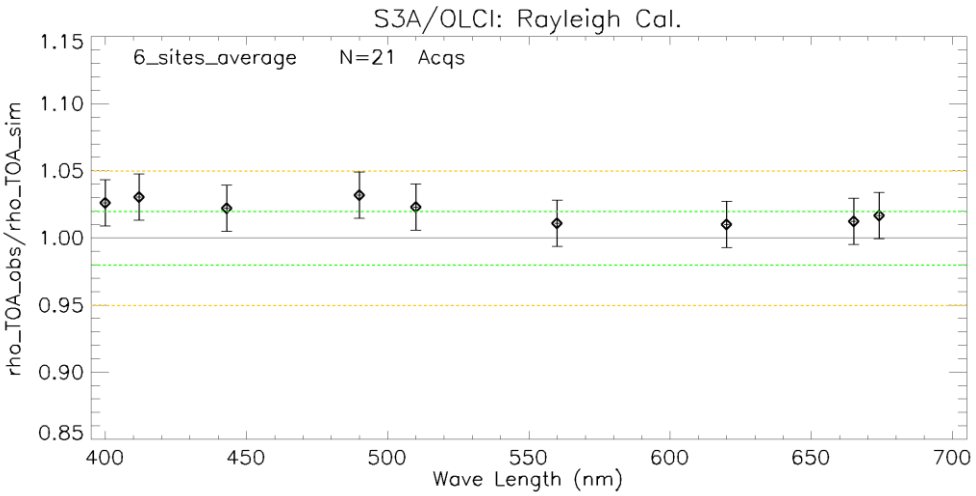

Figure 34: The estimated gain values for S3A/OLCI over the 6 Ocean CalVal sites (Atl-NW_Optimum, Atl-SW_Optimum, Pac-NE_Optimum, Pac-NW_Optimum, SPG_Optimum and SIO_Optimum) over the period December 2016 – October 2017 as a function of wavelength. Dashed-green, and orange lines indicate the 2%, 5% respectively. Error bars indicate the methodology uncertainty.

IV-Validation over Glint

Glint calibration method with the configuration (ROI-PIXEL) has been performed over the period December 2016 – end October 2017 from the available mini-files. The outcome of this analysis shows a good consistency with Rayleigh and the desert outputs over the NIR spectral range (see Figure 35).

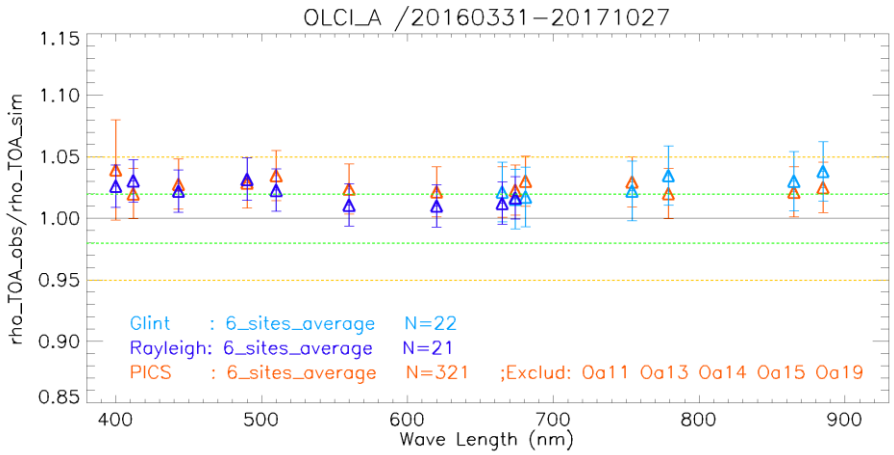

Figure 35: The estimated gain values for S3A/OLCI from Glint, Rayleigh and PICS over the period April 2016 – October 2017 for PICS and December 2016-October 2017 for Rayleigh and Glint methods as a function of wavelength. We use the gain value of Oa8 from PICS method as reference gain for Glint. Dashed-green and orange lines indicate the 2% and 5% respectively. Error bars indicate the methods uncertainties.

2.1.3 Radiometric validation with OSCAR

OSCAR Rayleigh results for August and September (preliminary results) are given in Figure 36. The weighted average result over all Rayleigh sites is given for observations with an airmass larger than respectively 2 and 3. As can be seen in the figure the selection of valid pixels based on the airmass has an effect in the first 3 OLCI bands which illustrates the larger uncertainty of the Rayleigh results in these 3 bands.

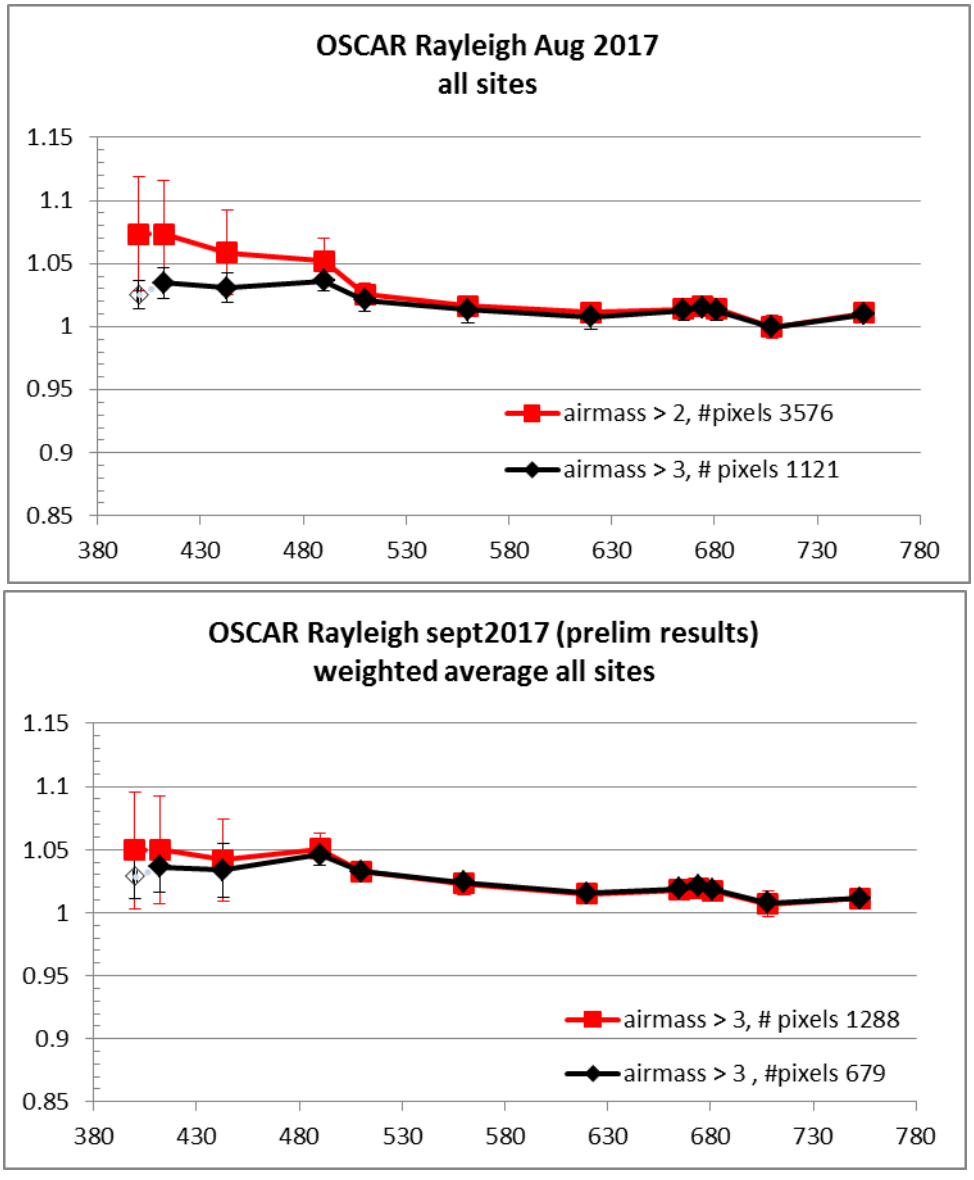

Figure 36: OSCAR Rayleigh results for August and September (preliminary) 2017.

2.2 [OLCI-L1B-CV-320] – Radiometric Validation with Level 3 products

There has been no new result during the cycle. Last figures (cycle 20) are considered valid

3 Level 2 Land products validation

3.1 [OLCI-L2LRF-CV-300]

In the frame of the validation of OTCI and OGVI, a specific study has been conducted regarding the impact of Cloud masking on the Land products

Seven different study areas were chosen for this study. They were chosen to cover a range of land cover conditions including; desert, bare soil, vegetated regions, tropical forests and an ice sheet. The imagery was downloaded from the Scihub data hub. Both L-1 and L-2 datasets were downloaded for each of the scenes.

Study Site	Date of product
France - Europe	28/09/2017
Los Angles - North America	25/09/2017
Queensland - Australia	02/10/2017
Denmark - Northern Europe	14/08/2017
Greenland	04/10/2017
Congo	30/07/2017
Rondonia – Brazil	27/08/2017

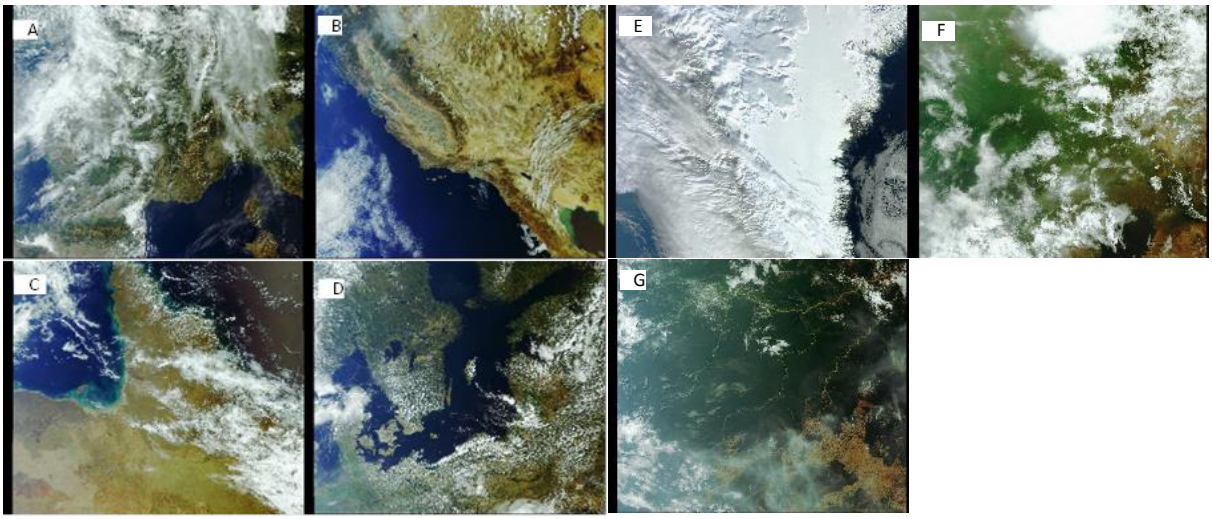

Figure 37: RGB composites of the study sites. A) France B) Los Angles C) Queensland, Australia D) Denmark E) Greenland F) Congo G) Rondonia

The total number of pixels identified by each of the different cloud masks can be seen within Table 2. The higher numbers within the Greenland image can be expected due to the difficulty in distinguishing cloud from snow using a coarse resolution imagery due to the similar spectral signals.

Table 2: Number of pixels identified by the different cloud masks within the images.

	Cloud	Cloud - Ambiguous	Cloud - Margin

	Number of pixels	% of image	Number of pixels	% of image	Number of pixels	% of image
	9745347	48.96%	141548	0.71%	2236645	11.24%
Los Angles - North America	2214502	11.13%	306970	1.54%	1750391	8.79%
Queensland - Australia	4824985	24.24%	174179	0.88%	2577830	12.95%
Denmark - Northern Europe	3777443	18.98%	193917	0.97%	4459148	22.40%
Greenland	14087467	70.78%	108262	0.54%	2744620	13.79%
Congo	9417263	47.32%	156567	0.79%	1870915	9.40%
Rondonia	1651842	8.30%	105872	0.53%	1272816	6.40%

One observation was that in some situations sections of inland water, such as rivers or edges of lakes, were being classified as cloud or cloud ambiguous pixels as well as inland water. The total number of pixels that were classified as both inland water and cloud can be seen within Table 3. The image focused over Denmark had the highest number of pixels identified within each of the different cloud masks. It is important to note, that in some instances the classification of both inland water and cloud was correct. However, there were instances, as seen within Figure 38**,** where the pixels were incorrectly identified as cloud. This had implications on OTCI estimates along the banks of rivers as additional pixels nearby were normally classified as ambiguous clouds and as such were removed from OTCI calculations. This issue was present within all of the images involved within the study.

Table 3: Number of pixels that were classified as both inland water and cloud.

	Inland water + Cloud	Inland water + Ambiguous cloud	Inland water + Cloud margin
France - Europe	81312	1766	16198
Los Angles - North America	33084	2053	26550
Queensland - Australia	13929	824	7044
Denmark - Northern Europe	120436	6264	110332
Greenland	71416	149	2069

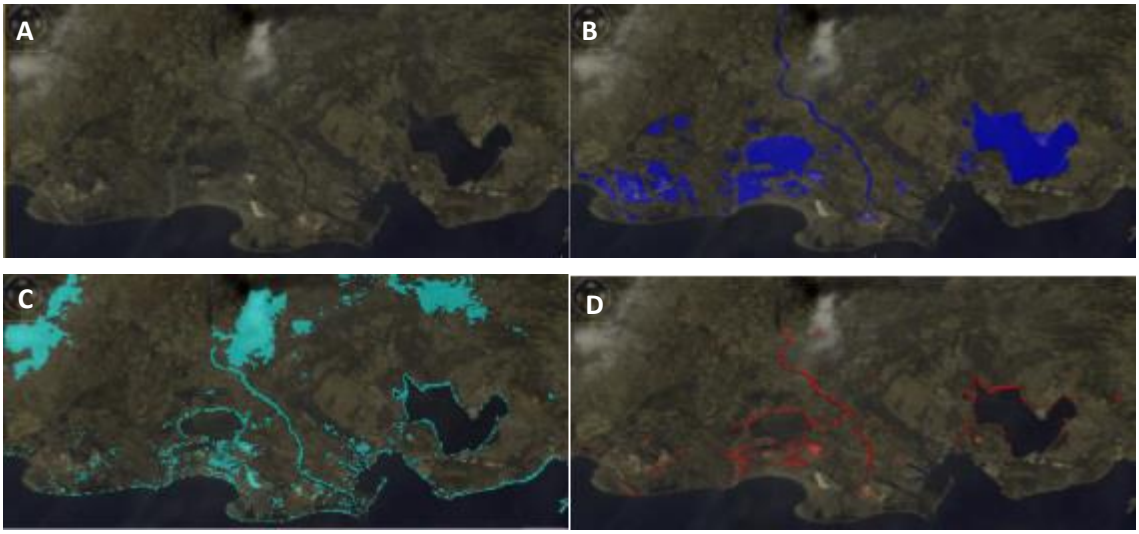

Figure 38: A) RGB image of the River Rhone, France (43°32'02" N, 4°43'06'' E). B) Inland water flagged pixels. C) Cloud flagged Pixels. D) Pixels classified as both inland water and cloud.

Within the Queensland imagery there were patches of cloud upon the edges of sections of cloud that were not being correctly classified by the cloud tagging. An example of this can be seen within Figure 39**.** Highlighted within the red square are areas of cloud that have not been detected, therefore OTCI values have been produced for these pixels as shown in Figure 39**.**

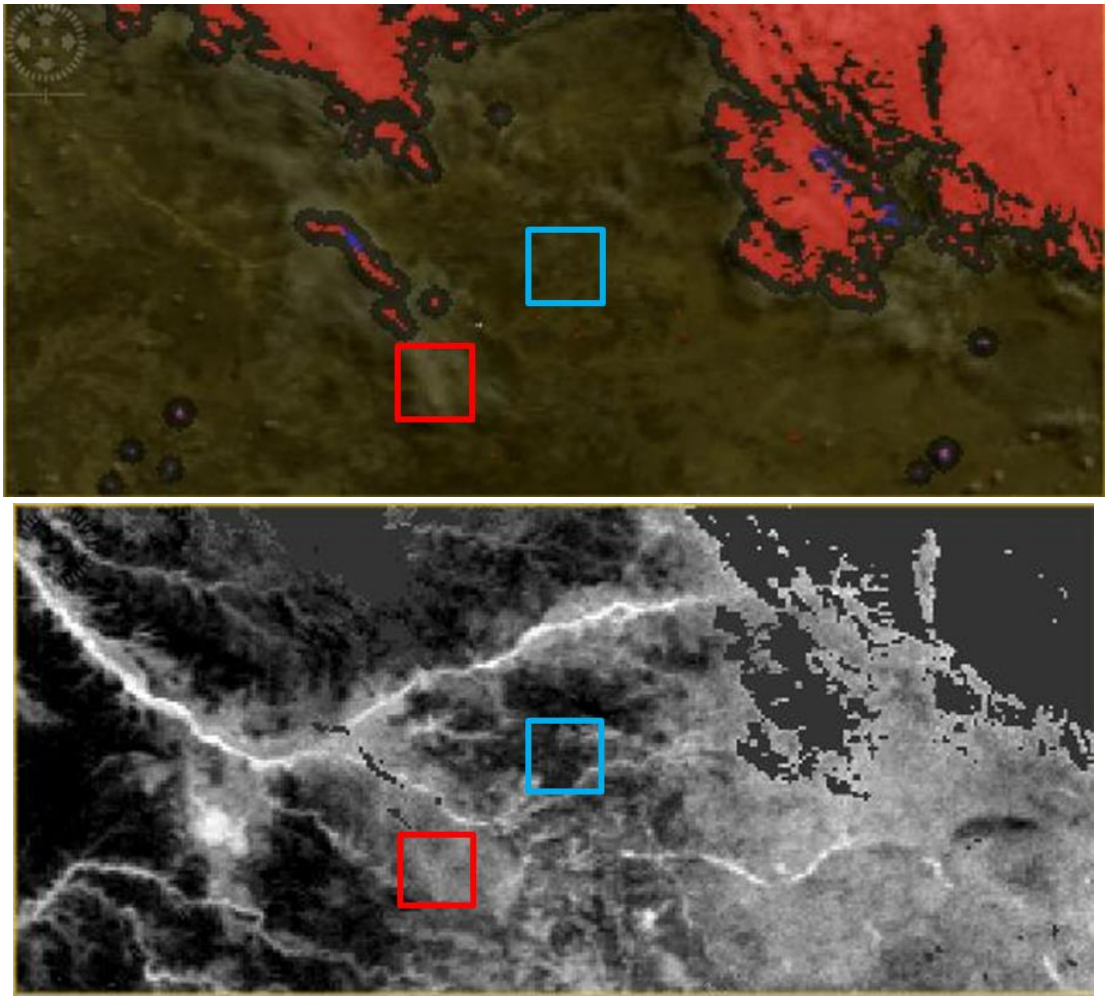

Figure 39: RGB and OTCI bands for Queensland Australia (17°26'04" S, 143°47'15" E).

50 pixels were selected from each of the areas identified in Figure 39. The blue square indicates an area of bare soil and the red square shows an area of cloud. The resulting histograms showing the spread of the different OTCI values recorded within these sections can be seen in Figure 40**.** The range of OTCI values is substantially lower for the section of cloud in comparison to the bare soil, with ranges of 0.23 and 0.51 respectively. This uniformity in OTCI values for the cloud can be seen within the histogram in Figure 40**.**

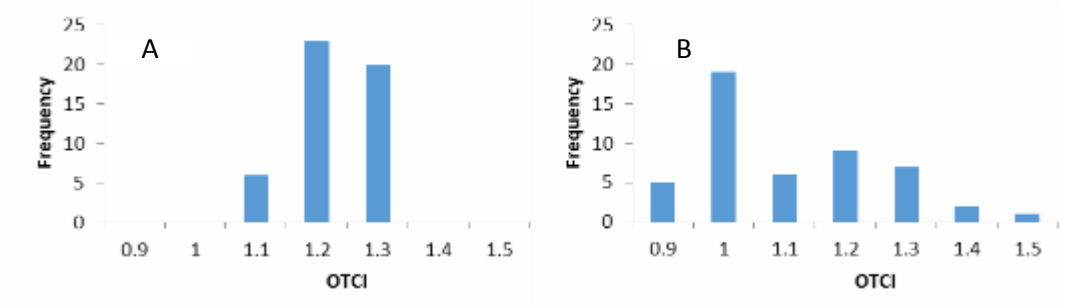

Figure 40: A) Histogram of OTCI values for cloud pixels. B) Histogram of OTCI values for bare soil pixels.

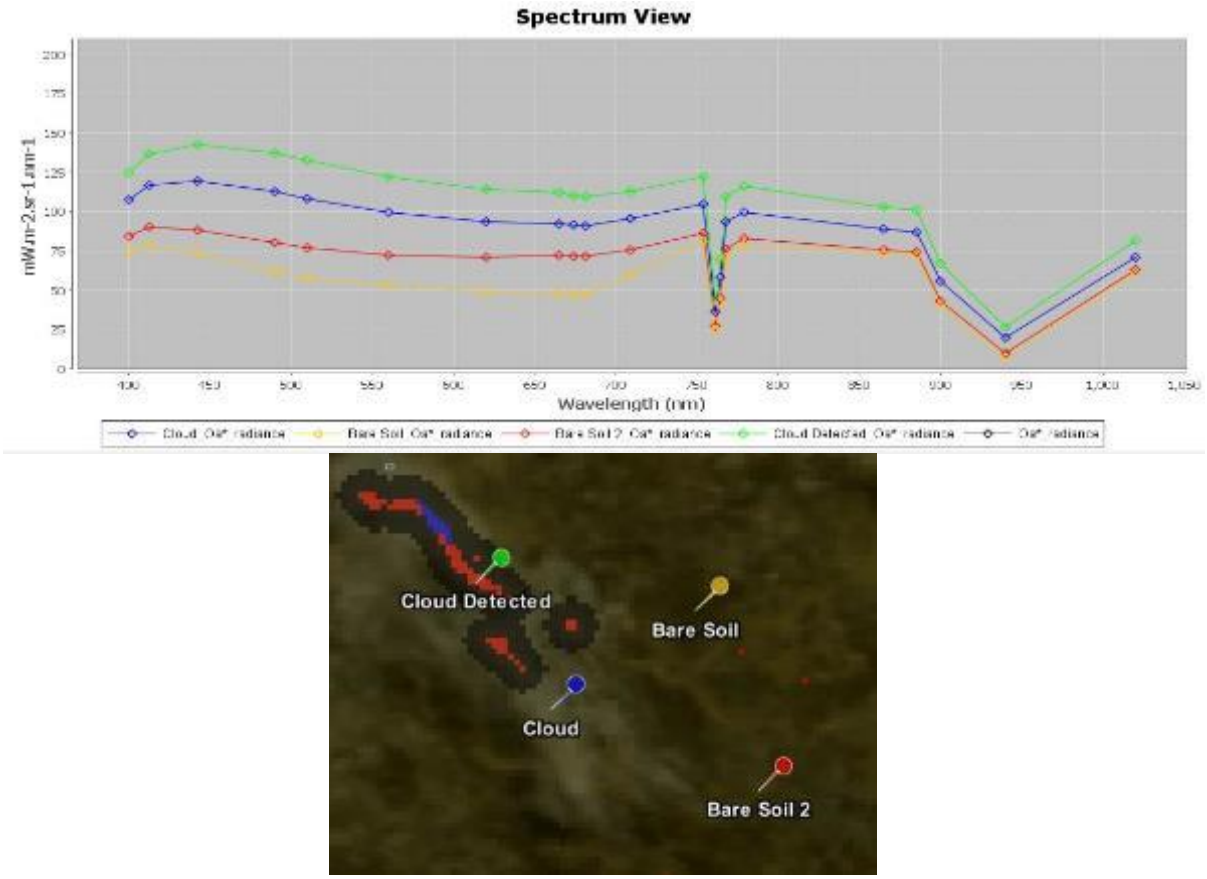

Figure 41: Spectral signals of the different classifications within the image Queensland Australia (17°26'04" S, 143°47'15" E).

The different spectral signals for different sections of the image can be seen within Figure 41. As can be seen there are at least two distinctive colours for the bare soil within the imagery resulting in slightly different spectra's. The spectra profiles of areas of identified cloud and non-identified cloud are similar in shape. Therefore, this shows that the thresholds for detecting cloud may need to be adapted to reflect the lower reflectance values obtained from cloud within the imagery.

Within the Los Angles image areas of bare soil were being misclassified as cloud when no cloud was present. An example of this is shown in Figure 42**.** This leads to pixels being unnecessarily removed from the OTCI band. The area that has been misidentified as cloud has a spectral signal that is closer to the soil spectra than the cloud spectra.

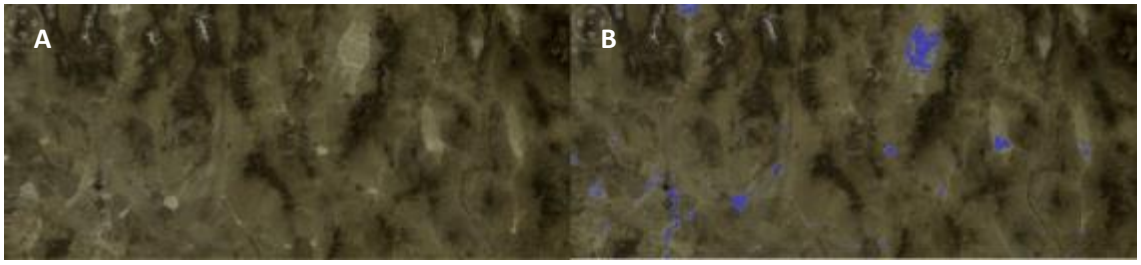

Figure 42: A) RGB image of Death Valley (38°13'40" N, 116°16'25" W). B) Cloud mask.

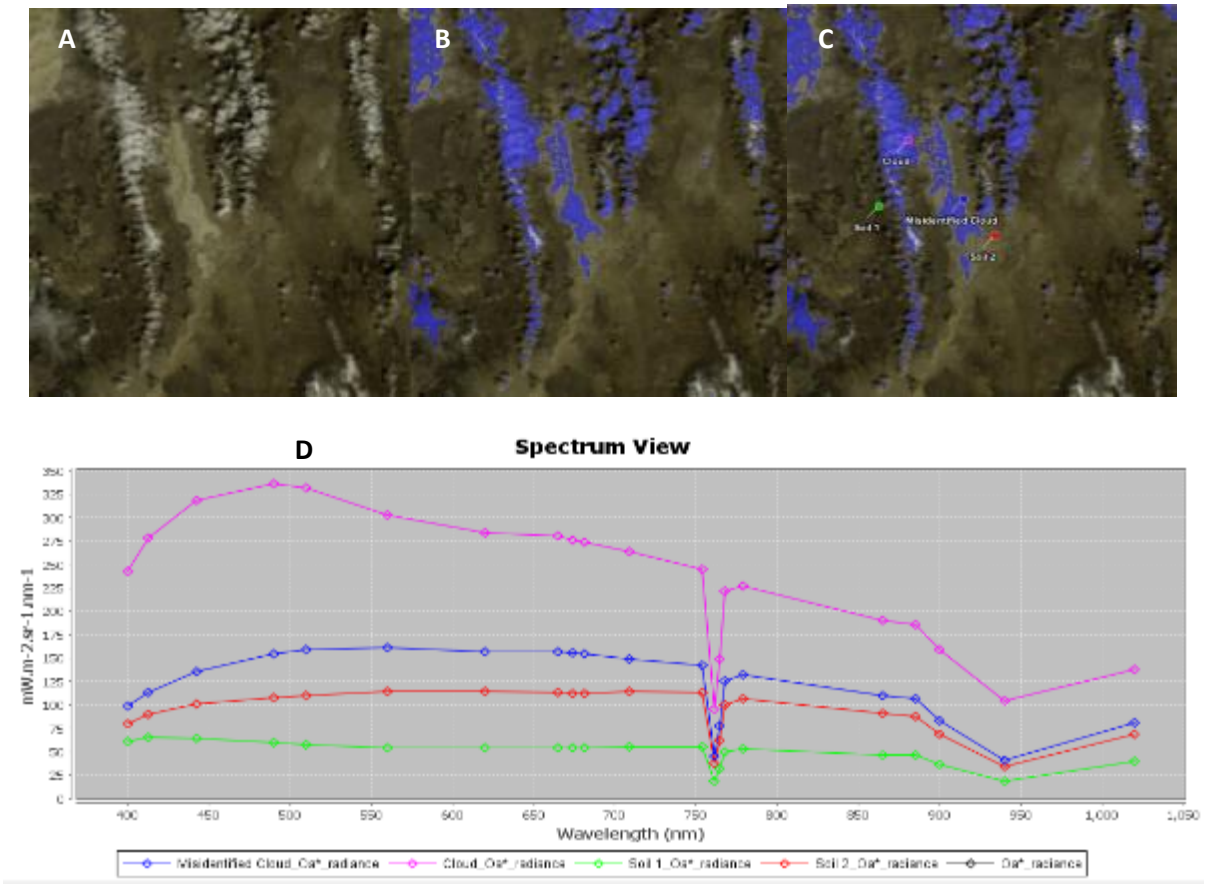

Figure 43: A) RGB composite (39°39'01" N, 115°54'46" W) B) Cloud mask C) Location of Pins. D) Spectral signals of the different pins.

Here only selected results were presented, UoS is further investigating this impact of thin cloud on OTCI.

3.2 [OLCI-L2LRF-CV-410 & OLCI-L2LRF-CV-420] – Cloud Masking & Surface Classification for Land Products

There has been no update on Cloud Masking & Surface Classification for Land t during the cycle. Last figures (cycle 20) are considered valid.

3.3 Validation of Integrated Water Vapour over Land

There has been no update on Integrated Water Vapour over Land validation quantitative assessment during the cycle. Last figures (cycle 15) are considered valid.

Qualitative assessment by product inspection showed no detectable performance evolution.

4 Level 2 Water products validation

4.1 [OLCI-L2-CV-210, OLCI-L2-CV-220] – Vicarious calibration of the NIR and VIS bands

There has been no update of the SVC (System Vicarious Calibration) during Cycle 023. Last figures (cycle 17) are considered valid.

4.2 [OLCI-L2WLR-CV-300, OLCI-L2WLR-CV-310, OLCI-L2WLR-CV-32, OLCI-L2WLR-CV-330, OLCI-L2WLR-CV-340, OLCI-L2WLR-CV-350, OLCI-L2WLR-CV-360 and OLCI-L2WLR-CV-370] – Level 2 Water-leaving Reflectance product validation.

Activities done

- The focus for this time period has been on the Near Real Time data from September 13th to November 4th 2017.
- All extractions and statistics have been regenerated fromSeptbember 13th onward (rolling archive limitation). The available matchups therefore cover the end of summer to fall situation. Time range available for last processing period covered July 1sh to September 7th time period
- An MPMF data provision failure has is not yet fully resolved. The amount of available data for routine validation is therefore very limited.
- Only a few matchups with AERONET-OC stations are available for this time period. These stations are located in optically complex waters (Black Sea, Gulf of Mexico and gulf of California). In addition, Aqua Alta Oceanographic Station hosting AERONET-OC AAOT is being fully refurbished and therefore do not provide any data.

Overall Water-leaving Reflectance performance

Figure 44 below presents the scatterplots with statistics of OLCI FR and RR versus in situ reflectance computed for the NT dataset. The data considered correspond to the latest processing baseline ie including SVC. Owing to the on-going data provision issue, very few OLCI images and therefore matchups are available for this reporting period. No reliable interpretation can be derived from these statistics. Table 4 to Table 10below summarises the statistics over the previous and current reporting. Overall data quality is nominal.

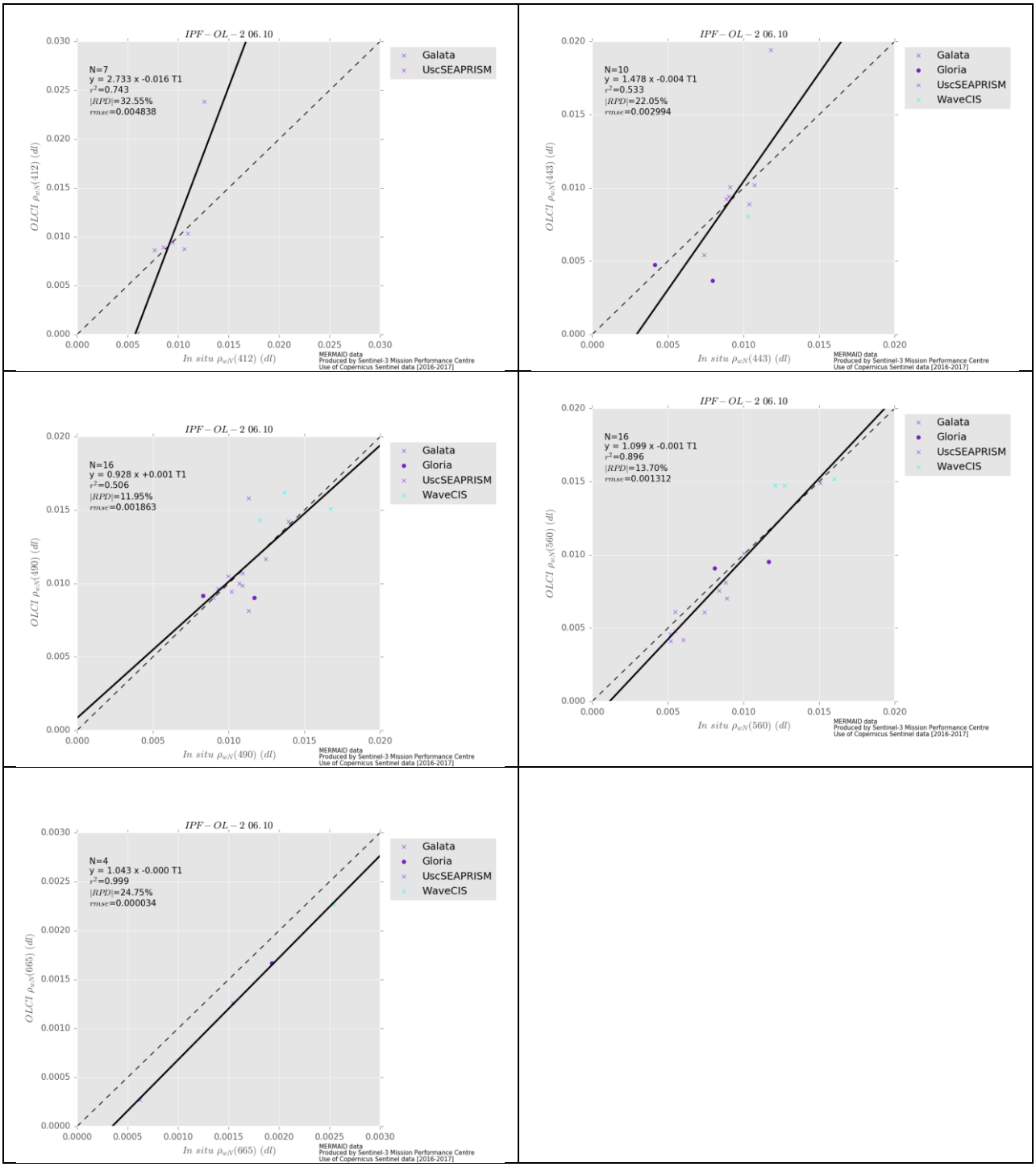

Figure 44: Scatter plots of OLCI versus in situ radiometry (FR data)

Table 4: FR statistics over December 2016-March 2017 reporting period

lambda	N	RPD	|RPD|	MAD	RMSE	slope	int.	r2
412	25	70,55%	77,47%	0,0055	0,0071	0,9486	0,0061	0,6787
443	25	43,34%	44,27%	0,0045	0,0056	1,1251	0,0028	0,9037
490	24	28,53%	28,53%	0,0048	0,0059	1,1634	0,0016	0,9611
510	2	31,69%	31,69%	0,0091	0,0093	2,0459	-0,0207	1,0000
560	17	15,44%	16,95%	0,0037	0,0052	1,1350	0,0003	0,9655
665	25	10,56%	34,24%	0,0010	0,0032	1,3661	-0,0013	0,9236

Table 5: FR statistics over February 2017-April 2017 reporting period

lambda	N	RPD	|RPD|	MAD	RMSE	slope	int.	r2
412	60	88.15%	93.77%	0.0052	0.0066	1.0404	0.0048	0.6176
443	60	46.70%	50.43%	0.0038	0.0049	1.1195	0.0026	0.8046
490	59	31.38%	32.56%	0.0039	0.0046	1.1397	0.0019	0.9263
510	19	27.06%	27.06%	0.0050	0.0055	1.1474	0.0021	0.9486
560	53	13.42%	16.58%	0.0024	0.0035	1.1281	0.0001	0.9379
665	51	1.02%	29.79%	0.0000	0.0012	1.0202	-0.0001	0.7892

Table 6 FR statistics over April 2017-June 2017 reporting period

lambda	N	RPD	|RPD|	MAD	RMSE	slope	intercept	r2
400	2	17.9%	17.9%	0.0088	0.0100	-2.3992	0.1784	1.0000
412	15	66.3%	66.3%	0.0055	0.0062	1.0618	0.0046	0.9611
443	15	36.7%	37.0%	0.0037	0.0044	1.1107	0.0023	0.9454
490	20	32.1%	32.3%	0.0038	0.0044	1.0153	0.0036	0.8224
510	10	35.9%	35.9%	0.0045	0.0048	0.8626	0.0064	0.7505
560	21	17.0%	21.9%	0.0020	0.0034	1.0925	0.0006	0.9205

Table 7: FR statistics over May 1st to July 10th reporting period

lambda	N	RPD	|RPD|	MAD	RMSE	slope	intercept	r2
412	35	30.5%	38.2%	0.0025	0.0060	0.9699	0.0033	0.9364
443	43	25.2%	32.9%	0.0023	0.0061	1.0444	0.0012	0.9546
490	52	15.2%	22.2%	0.0020	0.0055	1.0462	0.0007	0.9756
510	21	24.1%	24.9%	0.0026	0.0039	1.1577	0.0004	0.9946
560	52	2.4%	11.1%	0.0004	0.0045	1.0196	-0.0002	0.9701
665	32	-6.9%	17.7%	-0.0002	0.0023	0.9830	-0.0001	0.8423

Table 8: FR statistics over the current reporting period (July 11th to August 23rd)

lambda	N	RPD	|RPD|	MAD	RMSE	slope	intercept	r2
412	19	18.0%	32.2%	0.0008	0.0066	1.0075	0.0006	0.9346
443	24	10.2%	24.1%	0.0012	0.0072	1.0752	-0.0012	0.9524
490	32	8.0%	18.8%	0.0012	0.0062	1.0504	-0.0005	0.9743
510	10	17.6%	19.3%	0.0011	0.0014	0.9560	0.0014	0.6316
560	32	-1.0%	13.0%	-0.0002	0.0055	1.0179	-0.0008	0.9618
665	22	-10.8%	18.4%	-0.0004	0.0027	0.9028	0.0003	0.7552

Table 9: FR Statistics over the current reporting period (July 1sh to September 7th)

lambda	N	RPD	|RPD|	MAD	RMSE	slope	intercept	r2
412	6	81.5%	95.7%	0.0017	0.0064	0.6848	0.0063	0.7589
443	7	31.6%	49.7%	0.0003	0.0041	0.8661	0.0026	0.9401
490	11	5.8%	20.1%	0.0003	0.0022	0.9909	0.0004	0.9818
510	3	13.0%	20.2%	0.0009	0.0015	1.1289	0.0000	0.1477
560	11	-4.5%	12.9%	-0.0009	0.0021	0.9270	0.0004	0.9784
665	7	-22.5%	22.5%	-0.0008	0.0009	1.0191	-0.0009	0.9618

Table 10: FR Statistics over the current reporting period (September 13th to November 4th)

lambda	N	RPD	|RPD|	MAD	RMSE	slope	intercept	r2
400	0	None	None	None	None	None	None	None
412	7	-2.1%	32.6%	0.0006	0.0049	2.7334	-0.0157	0.7427
443	10	-2.2%	22.0%	-0.0001	0.0030	1.4778	-0.0043	0.5329
490	16	0.4%	11.9%	0.0000	0.0019	0.9282	0.0008	0.5065
560	16	-5.9%	13.7%	-0.0004	0.0014	1.0994	-0.0013	0.8961
665	4	-24.8%	24.8%	-0.0003	0.0003	1.0428	-0.0004	0.9994

Figure 45 below shows illustrate the lack of both is situ and OLCI data on the current reporting period..

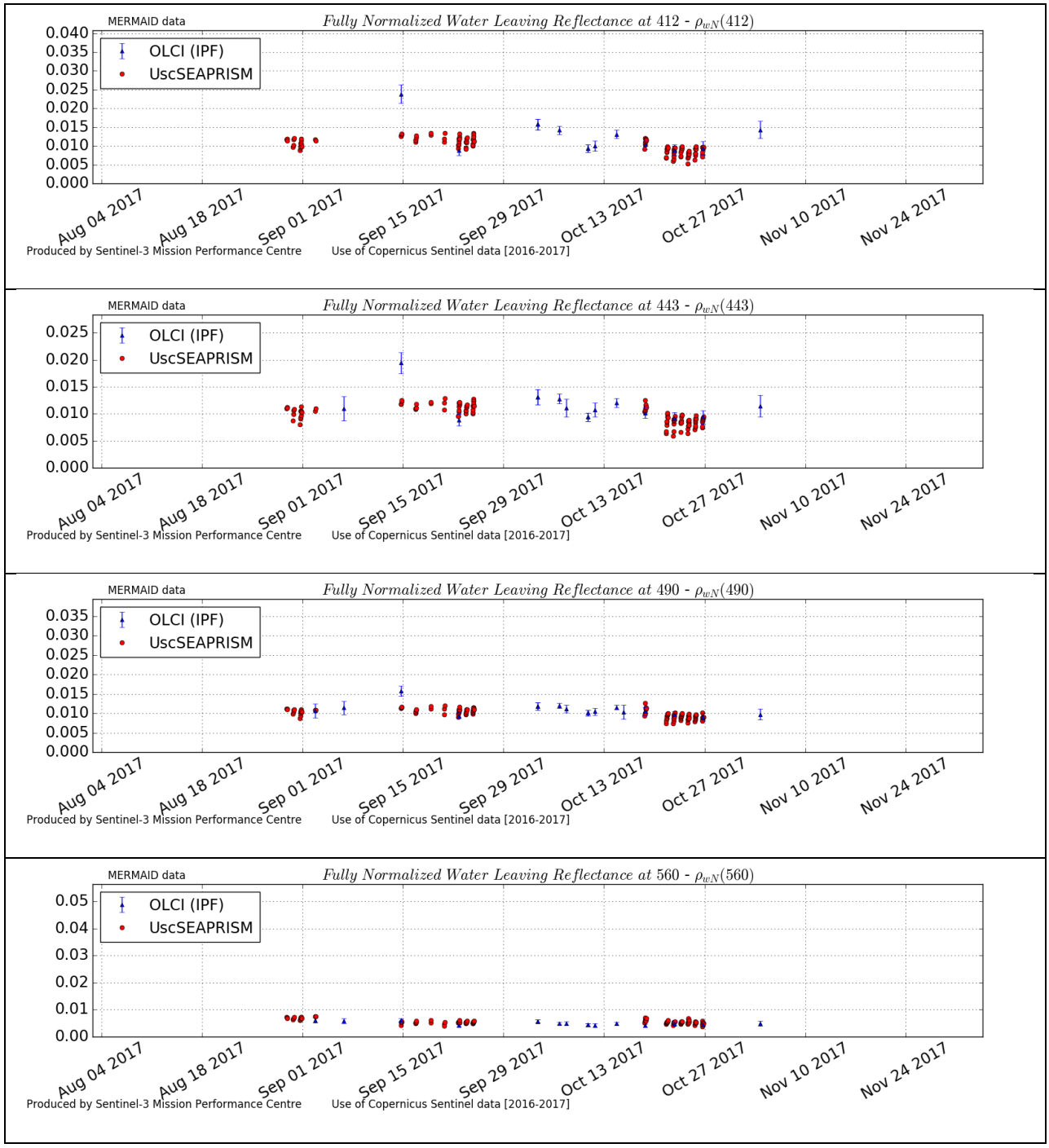

Figure 45: OLCI and AERONET-OC radiometric time on USCSeaprism station.

4.3 [OLCI-L2WLR-CV530] Validation of Aerosol Product

There has been no update on Aerosol Products validation quantitative assessment during the cycle. Last figures (cycle 18) are considered valid.

Qualitative assessment by product inspection showed no detectable performance evolution.

4.4 [OLCI-L2WLR-CV-380] Development of calibration, product and science algorithms

There has been no new developments on **calibration, product and science algorithms** during the cycle

5 Level 2 SYN products validation

5.1 [SYN-L2-CV-100]

There has been no new result during the cycle. Last figures (cycle 21) are considered valid

6 Events

Two OLCI Radiometric Calibration Sequences have been acquired during Cycle 023:

- S01 sequence (diffuser 1) on 04/10/2017 07:58 to 08:00 (absolute orbit 8492)
- S01 sequence (diffuser 1) on 21/10/2017 10:41 to 10:43 (absolute orbit 8736)

An anomaly occurred on OLCI on 16/01/2017 around 2:00 UTC, resulting in corrupted data of camera 4. The corruption affected not only the science data but also the Source Packets headers and in particular some fields of the channels definitions that are checked against their reference from an ADF. Consequently all Packets of camera 4 were rejected and the Level 0 to Level 1 processing failed.

The anomaly has been resolved the same day and nominal OLCI data was acquired and transmitted to ground from 12:00 UTC on.

7 Appendix A

Other reports related to the Optical mission are:

- S3-A SLSTR Cyclic Performance Report, Cycle No. 023 (ref. S3MPC.RAL.PR.02-023)

All Cyclic Performance Reports are available on MPC pages in Sentinel Online website, at: https://sentinel.esa.int

End of document